Ion Beam Figuring Technology

36

Xuhui Xie and Shengyi Li

Contents

Abstract

In deterministic figuring process, it is critical to guarantee high stability of the removal function as well as the accuracy of the dwell-time solution, which directly influences the convergence of the figuring process. As an ultraprecision optical machining technique, ion beam figuring (IBF) has unique features, such as a highly controllable, stable, and noncontact material removal process, atomic

X. Xie (✉) • S. Li
College of Mechatronic Engineering and Automation, National University of Defense Technology (NUDT), Changsha, Hunan, People's Republic of China
e-mail: xuhuixie67@sina.com; syli@nudt.edu.cn

A.Y.C. Nee (ed.), *Handbook of Manufacturing Engineering and Technology*,
DOI 10.1007/978-1-4471-4670-4_65

scale material removal capability, etc., well to satisfy this requirement. Currently, IBF is widely used to machine ultraprecision optical elements which is used in lithography, space observation, and so on. This chapter has three sections to describe the IBF technology. Some important research results, summaries, and applications come from our research group. The fundamental theory of IBF is introduced firstly, which includes its principles, its distinctive performances and advantages, the current status and future of IBF, etc. The main content of this chapter is to discuss the key technology of IBF, such as material removal function modeling, contouring algorithm, analysis of correcting ability, optimum material removal of IBF, realization of IBF technique, and so on. In the third section, the challenges of IBF technical development and its new applications are also discussed in detail. They are (1) high-gradient optical surface figuring by IBF, (2) high thermal expansion and crystal optics figuring by IBF, and (3) supersmooth surface figuring and micro-roughness evolution. Finally, some conclusions and suggestions are summed.

Introduction

The classical process chain for the fabrication of precision optical component consists of three steps. (1) The generating process includes grinding and milling, which is used to generate a precision optical surface with micrometer range of contour accuracy but still with microscopic roughness. This process is so-called optical surface forming (shaping). (2) The polishing process is used to remove roughness, subsurface damage, and surface error under corrective improvement of the shape accuracy by speed/pitch polishing. After this process, the surface usually has been smoothed to optical quality, but it is difficult or time-consuming to reach the specified surface accuracy since tool wear, edge roll-off effect, force loading of workpiece, etc. (3). The surface finishing process is a necessarily additional step to deterministically correct the surface contour to its desired accuracy. The main role of this process is to further improve the surface accuracy. In this process, the typical machining methods include CCOS (computer-controlled optical surfacing), MRF (magnetorheological finishing), IBF (ion beam figuring), and so on. The ion beam figuring (IBF) has the best machining precision. The characteristic features of each process step are listed in Table 1 (Braunecker et al. 2007).

Fundamental Theory of IBF

Principles of IBF

Ion beam figuring (IBF) is a technique used for removing material from a surface by transferring kinetic energy from impinging neutral particles which is a nonabrasive technique for fine correcting the contour of precision optics. This figuring process utilizes a Kaufman-type ion source where plasma is generated in a discharge

Table 1 Overview characteristics of different processes (typical in production)

Process	Shape deviation (nm)PV	Surface roughness (nm)RMS	Advantage	Limits
Grinding	1,000	50–1,000	Fast generating process	Subsurface damage
Speed/ pitch polishing	300	0.2–0.5	Very low surface roughness, fast polishing process	Correction of local surface deviation
CCOS	30	0.5	30 years experience	Tool wear, edge roll-off
MRF	10	0.3	No edge roll-off, no tool wear, low damaged surface	Center artifact for γ–φ tool path
IBF	5	0.2	No edge roll-off, no tool wear, no damaged surface	Low removal rate, vacuum

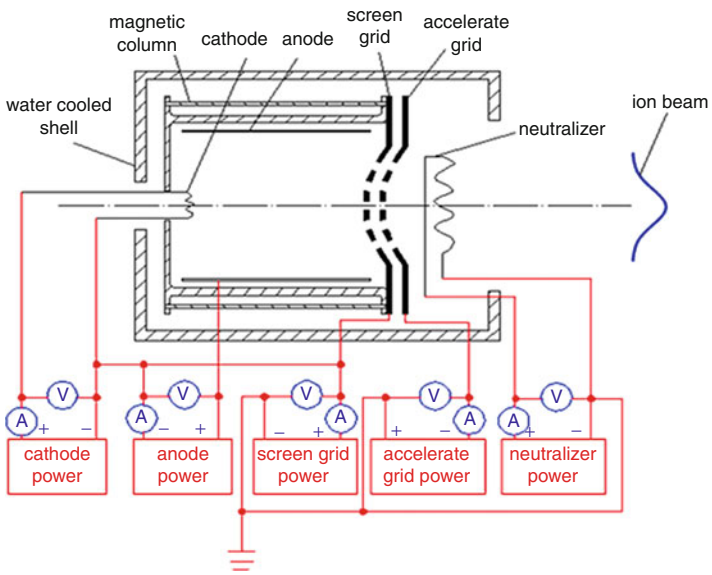

Fig. 1 Scheme of Kaufman ion source

chamber by controlled electric potential (Kaufman et al. 1977). Its sketch graphic is shown in Fig. 1, where charged concave-type grids extract and accelerate ions from the chamber. The accelerated ions form a directional ion beam with Gaussian-type distribution. A neutralizer outside the grids supplies electrons to the directional ion beam to necessarily neutralize the beam to prevent charging optical component and to avoid bending the beam by extraneous electromagnetic fields from a charged workpiece or from other source. When the ion beam hits the optical component,

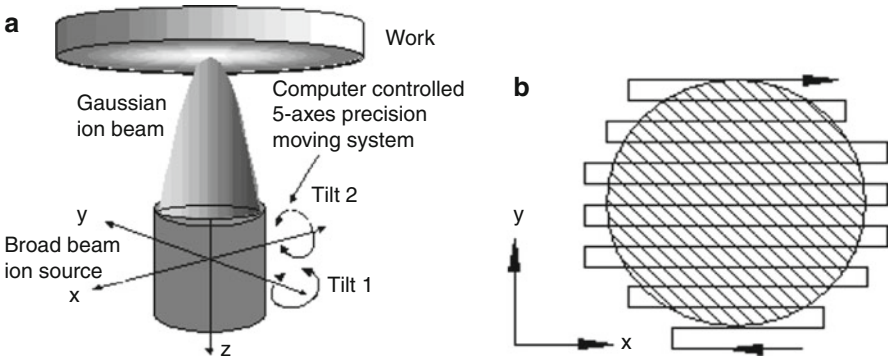

Fig. 2 Scheme of the IBF process

the amount and distribution of material sputtered is a function of the material of optical component, the incidence energy, distance, and angle of ion beam (Sigmund 1973; Bradley and Harper 1988).

In IBF process, a non-varied ion beam energy maintains a constant sputtering rate (or material removal rate) and profile which is very important for optical deterministic figuring method to gain a constant beam removal function. Then, this temporally and spatially stable ion beam is held perpendicular to the optical surface at a fixed distance with ion source controlled by a 5-axis CNC system shown in Fig. 2 (Ion Beam Finishing Technology for High-Precision Optics Production). The optical deterministic figuring method described here is assumed a constant beam removal, so that the process can be represented by a convolution operation based on the CCOS (computer-controlled optical surfacing) theory. If not a constant beam removal, its corrections would be required to model the process which will be discussed in the section "High-Gradient Optical Surface Figuring by IBF."

The Typical Features and Its Purpose of IBF

Using ion beam to figure optical component, it has the following features and advantages:

1. High figuring precision. Based on the physical sputter effect, the material removal rate is in molecular or atomic level, so IBF figuring precision can be maintained in nanometer or sub-nanometer precision in the condition of ion beam stability.
2. Highly predicable and stable. Compared with traditional abrasive optical figuring methods, where chemical interaction (hydrated layer) and mechanical interaction (scratching) remove the material of optical component, IBF is figuring with ions, such as argon, which is like sandblasting. Its sputter rate can be accurately calculated by the physical law of elastic and inelastic scattering. Since no a chemical interaction, ion beam parameters that can be easily held

in constant are the main reasons for the stability of IBF process. These features make the figuring process highly predictable and stable. That allows the figuring process to rapidly converge to the desired specifications and save significant time and cost.

3. Noncontact figuring. The noncontact nature eliminates the problems of tool wear, edge roll-off effect, loading force on the workpiece, and surface/subsurface mechanic damage generated by mechanical interaction in the conventional grinding and polishing methods. This feature is very useful for figuring very thin and lightweight optical component.
4. Good material removal function. The two main advantages of material removal function are Gaussian distribution and constant profile. The Gaussian distribution removal function is an ideal function for figuring process which can simplify the dwell-time calculation and improve figuring precision.
5. No or minimized support structure print effect. The so-called support structure print effect is the honeycombed support structure of the back side that is visible on the front optical surface for lightweight structure optical component, such as lightweight SiC optics. This is troublesome problem for traditional figuring process because of the loading force impact.

In addition, the ion beam figuring process is a clean figuring process which avoids the influences of polishing liquid and polishing abrasive in the conventional figuring process which usually lead to generate redeposition layer and insert polishing abrasives. IBF is an excellent complement to conventional figuring to gain very high optical surface and subsurface quality. However, it has some shortcomings, such as working in a vacuum chamber; component heating because the ions hit the optical surface with several hundreds to thousands eV, some of them being stopped by absorption which heats the workpiece; difficulty of improving surface roughness because of the ion "sandblasting" effect at the atomic level (recent work suggests that it could even be used to improve the roughness); slow material removal rate with normal values from tens to several hundreds nanometer per minute; etc.

Description of IBF Process

The basic flow of IBF process is shown in Fig. 3. Prior to any figuring, the material removal function (shown in Fig. 3) must be determined for the process as it is the base of deterministic figuring process. About how to gain this function, its detail will be discussed in the section "Removal Function Modeling and Analyzing of IBF." The material removal function (or called beam function), analogous to a point spread function, provides a depth removal rate distribution as a function of radial distance from the ion beam center.

The ion beam figuring process begins with measuring the contour of the optical component by interferometer, such as ZYGO series of interferometer, which results in an x–y array map of relative surface height values. Then to gain a removal map,

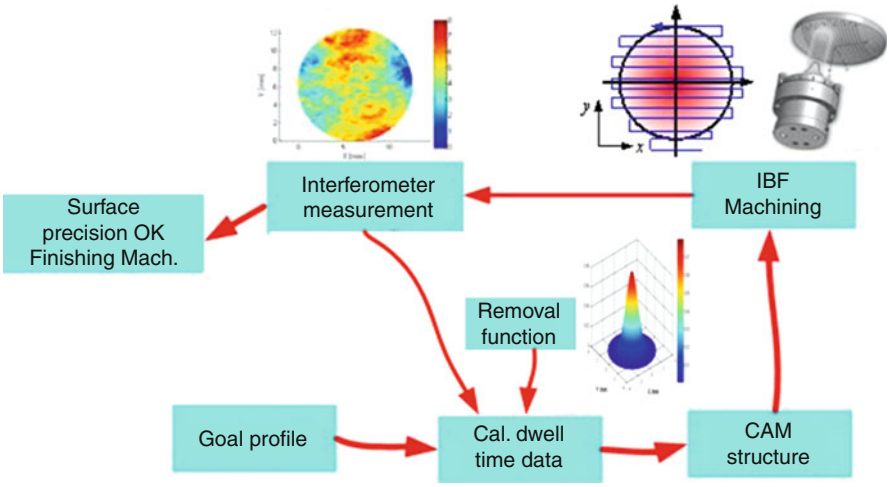

Fig. 3 Flow of IBF process

the difference between the measured surface contour and the goal surface contour, it describes the material to be removed. Based on the removal function and removal map, a dwell-time calculation is the third step in this flow. In CAM step, its one aim is to make the ion beam moving routine and its velocities to realize dwell function according to the machine motion performance, such as axial maximal velocity and acceleration. The other aim is to automatically generate control codes or NC codes to the CNC system when the controller of an IBF machine is a standard CNC system. For figuring, the optical component is placed in the vacuum chamber, and the ion beam raster scans over the surface of optical component according to the dwell time and the moving routine. In the IBF process, the material removed and its distribution are represented by the convolution of the removal function and the dwell time:

$$R(x, y) = B(x, y) * T(x, y) \tag{1}$$

where $R(x, y)$ is the material to be removed, $B(x, y)$ is the material removal function, and $T(x, y)$ is the dwell time. If the material to be removed and a material removal function of ion beam were known, the dwell time could be solved by deconvoluting Eq. 1. This is the fundamental of IBF process.

There are some key problems that would be paid more attention to realize IBF and gain good figuring results. They are listed as (1) how to select suitable sizes and beam parameters of ion beam that is very important to control the low-, middle-, and high-spatial-frequency errors of surface contour; (2) how to correctly evaluate the material removal function; (3) how to reasonably process the measuring contour data to make ion beam move smoothly as soon as possible to decrease the high-spatial-frequency errors generated; and (4) how to plan suitable ion beam moving routine including the suitable velocity, acceleration, pitch of raster scanning, and so on. Those four problems will be discussed in detail in the section "The Key Technology of IBF."

Current Status and Future of IBF

The earliest work is done by Meinel et al. (1965), which is the first report to apply ion beam to polish optical glass. Since the over high beam energy generated by ion source, the polished glass surface was seriously damaged. The subsequent successful work on IBF should firstly thank Kaufman who invented a new low-energy ion source, so-called Kaufman ion source. Early work on IBF was re-performed using Kaufman ion source by Gale at the end of 1970s (Gale 1978). This work was deeply expanded at the University of New Mexico in the USA by S. R. Wilson et al. (1987, 1989). They did many initial figuring experiments on fused silica, Zerodur, and copper optical component with 2.54 cm Kaufman ion source. Their representative result is to figure a 30 cm fused silica optics from contour precision 0.41λ RMS to 0.042λ RMS ($\lambda = 632.8$ nm) in one figuring cycle with 5.5 h. Lynn N. Allen et al. originally developed IBF system at the Eastman Kodak Company in 1988 and became operational in 1990 (Allen and Keim 1989; Allen and Roming 1990). This IBF system is designated for figuring large optics with up to 2.5 m × 2.5 m × 0.6 m of sizes. There are about 65 segments of 10 m Keck primary mirror was successfully realized their final figuring with 15 months. And 14 segments of them were measured after final figuring. Their average figuring accuracy was improved from 0.347 μm to 0.062 μm, and the maximal one-cycle error convergence ratio is 17.5 and the average value 5.6. The highly efficient figuring capability of IBF was successfully shown in Kodak Company which opened a new era for optical figuring technology (Allen and Roming 1991; Allen and John 1991).

Another representative work is the new Precision Ion Machining System (PIMS) research facility at NASA's Marshall Space Flight Center at the beginning of 1990 (Drueding 1995), which is focused on the figuring of small optics using 3 cm ion source. Since the ratio of ion beam to the size of small optics is greater, figuring a smaller optics is more difficult. Currently, the small optics figuring by IBF is also an interesting and valuable research work in optical figuring (Fawcett 1994; Shanbhag et al. 2000).

Besides the above work, there many IBF systems were setup at the end of 1990s, such as CSL lab in Belgium (Tock et al. 1999), IOM & NTG in Germany (Fruit et al. 1999; Schindler et al. 2000), INAF–OAB in Italy (Ghigo et al. 2001), and so on. Cannon Co. Ltd in Japan set up its IBF system for EUVAL in 2004 (Ando et al. 2004). NUDT (National University of Defense Technology) in China set up a series of IBF system in 2006, 2010, and 2011 (Lin et al. 2007; Yuan et al. 2011). One of these IBF systems is listed in Fig. 4. In addition, INAF–OAB in Italy and REOSC in France set up large IBF systems for 1.7 m- and 2 m-diameter space optics fabrication, respectively (Ghigo et al. 2009; Roland 2010). And also a large IBF for figuring 1.6 m diameter optics is building in the NUDT of China.

Currently, IBF method is universally used to fabricate ultrahigh-precision optical component, such as optics of DUV and EUV lithography, large space optics that many of them are the stitched primary optics whose segments are required no or very small error of edge roll-off effect. The interesting and focus research contents mainly include (1) figuring supersmooth optics, in which their key problems are

Fig. 4 One of IBF systems in NUDT

how to control the middle- and high-spatial-frequency errors and how to hold or improve the surface roughness; (2) dwell-time calculation and figuring technique; (3) the heat effect control that is very serious for high thermo expand material and crystalline, such as BK7, BK9, CaF_2, etc.; and (4) the optical material fabrication properties. The surface properties of the optical component influence the effectiveness of the process, and on the other hand, not all of the optical material can be figured by IBF.

The Key Technology of IBF

The computer-controlled optical surfacing (CCOS) method is a deterministic optical fabricating method based on the known figuring process model. Its ideal figuring process is based on the following several assumptions:

1. Material removal is linear and proportional to the dwell time.
2. Respective material removal rate is constant over the entire surface.
3. Material removal function is non-variant with time.
4. Material removal function is insensitive to position on the optical surface.

Analyzing these assumptions, the core is to gain a desired non-variant material removal function or to know its varied property. For conventional deterministic figuring processes, it is very difficult to know a precise material removal function because of some of the physical constraints, such as optic geometry and construction, aspheric departure, tool wear, edge roll-off effect, and loading force on optical

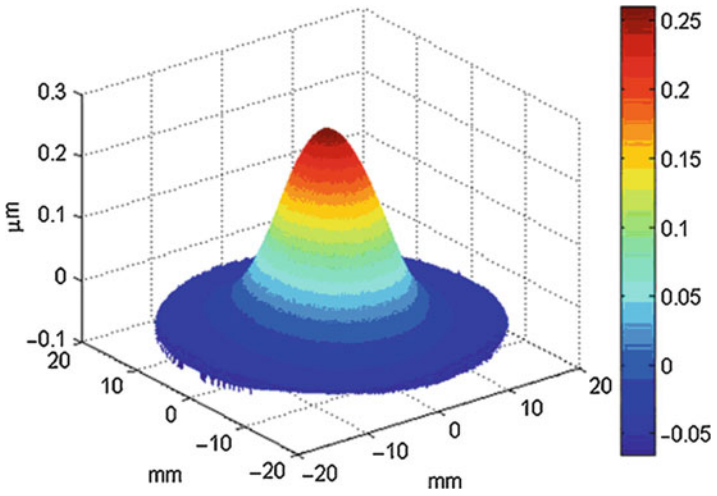

Fig. 5 A typical material removal function of IBF

component. These constraints limit the fabricated error convergence rate and the final fabricated contour accuracy. With IBF, it is nearly independent of the above constraints since the "figuring tool" is a noncontact and controllable compliant tool (Shengyi and Xuhui 2010). It is can be said that the IBF is reasonably valid to these assumptions in a wide range of material applications which is proved by many actual applications. It is acknowledged as the most deterministic optical figuring method.

Removal Function Modeling and Analyzing of IBF

In IBF, a typical material removal function (or called beam removal function, BRF) $b(x, y)$ shown in Fig. 5 is defined as the material removal profile or "footprint" on optical surface generated by the projected ion beam per unit time. In most cases, the removal function distribution is a circular Gaussian shape, which is dependent of the ion beam size and intensity, the bombarded material. When these are determined, the removal function can be described as (Lin et al. 2007)

$$b(x, y) = A \cdot e^{-\frac{x^2+y^2}{2\sigma^2}}. \tag{2}$$

where A is the peak removal rate and σ is the Gaussian parameter. It can be also expressed as

$$b(x, y) = \frac{B}{2\pi\sigma^2} e^{-\frac{x^2+y^2}{2\sigma^2}}. \tag{3}$$

where B is the volumetric removal rate; it can be calculated by

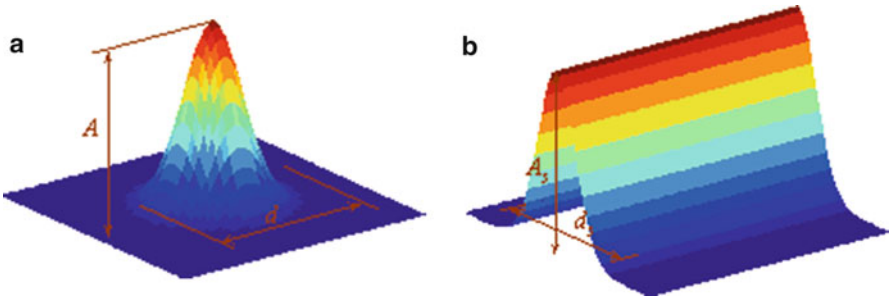

Fig. 6 Evaluating parameters of Gaussian-type removal function

$$B = \int_{-\infty}^{\infty} dx \int_{-\infty}^{\infty} b(x, y) dy. \tag{4}$$

B is in unit of μm · mm^2 · min^{-1}. It means the volumetric removal of the BRF, and

$$B = 2\pi\sigma^2 A. \tag{5}$$

There are two kinds of method to determine a BRF. One is an empirical method by optical or electro-probing. The electro-probing method is used to measure the ion beam current distribution by Faraday cup to get a BRF profile; its drawback is not to contain the correlation with the actual removed material, but it is a good method to regularly monitor the stability of BRF in the actual figuring process. Compared with this method, that of the optical probing is more efficient because it directly uses the ion beam to locate and bombard an optical surface in a given time to generate a "footprint." The BRF mathematical expression is obtained from the real interferometric evaluations to this "footprint." The other is mathematical method based on the ion sputtering theory.

With the optical probing method, the key problem is to correctively evaluate the parameters of Gaussian-type BRFs: A, σ (or d), and B, as shown in Fig. 6a. There are two ways to do this. The common way is to hit 4–8 "footprints" on an optical planar surface and then to evaluate the BRF Gaussian-type function with the average of these "footprints." Another way is to scan a trench on planar optical surface with travel speed v (mm · min^{-1}) and hold the ion source parameters constant; the transverse material removal profile along the trench can be approximated as a Gaussian function $r_s(y)$ as shown in Fig. 6b:

$$r_s(y) = A_s e^{-\frac{y^2}{2\sigma_s^2}} \tag{6}$$

where it is assumed that the ion beam scanning direction is x and its transverse direction is y. σ_s is the standard deviation; it equals to σ:

$$\sigma_s = \sigma. \tag{7}$$

The peak removal rate A_s is

$$A_s = \frac{1}{v}\sqrt{2\pi}\sigma A \tag{8}$$

$$A = \frac{v}{\sqrt{2\pi}\sigma}A_s. \tag{9}$$

Therefore, the BRF key parameters A and σ can be estimated by the trench transverse profile parameters A_s and σ_s in Eqs. 6–9.

The volumetric removal rate B can also be estimated as

$$B = v\sqrt{2\pi}\sigma_s A_s. \tag{10}$$

However, the estimated B is less believable because of the estimated errors of A_s and σ_s. So, a better method to estimate the volumetric removal rate B is to define $r_s(y)$ as

$$r_s(y) = \frac{B}{v\sqrt{2\pi}\sigma_s} e^{-\frac{y^2}{2\sigma_s^2}}. \tag{11}$$

The both sides integral form of Eq. 11 is

$$\int r_s(y)dy = \frac{B}{v}. \tag{12}$$

Then, B can be estimated by

$$B = v \cdot \int r_s(y)dy. \tag{13}$$

Here, $r_s(y)$ is the interferometric data of the trench transverse profile. It is proved that it is more precious to calculate B with Eq. 13 than that of Eq. 10. The other advantage with this method is that the uncertainty of RBF can be evaluated at the same time by analyzing the scatters on the width and depth of the profile of trench.

The mathematical method to model the material removal function is based on the Sigmund sputtering theory (Sigmund 1973). According to this theory, the energy deposition of incident ions follows a Gaussian distribution as shown in Fig. 7. The energy deposition at point O as the result of cascade collision when ions hit the surface at point A and travel along the z-axis can be written as

$$E = \frac{\varepsilon}{(2\pi)^{3/2}\sigma\mu^2}\exp\left(-\frac{(z+a)^2}{2\sigma^2} - \frac{x^2+y^2}{2\mu^2}\right) \tag{14}$$

where (x, y, z) is a coordinate system with origin at the energy deposition center and the z-axis along the projected path, ε is the total energy deposited, a is the average incidence depth of the ions, and σ and μ are the Gaussian distribution parameters along and transverse to the beam direction, respectively.

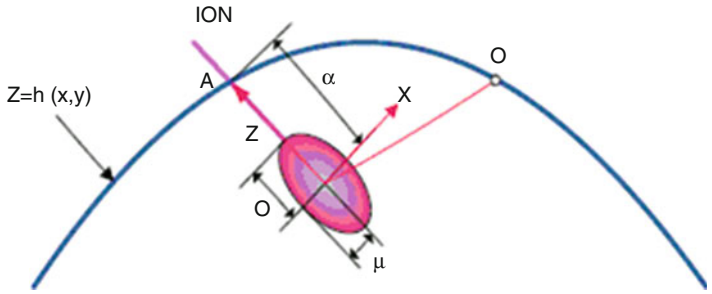

Fig. 7 The sketch map of energy deposition

It is known that the material removal rate and profile relate to the parameters of the IBF process. Besides these, they also are influenced by the curvature of optical surface and the beam incidence angle which would be paid attention in the fine figuring process. With Sigmund sputtering theory, Bradley and Harper deduced the etching rate on an arbitrary surface $z = h(x, y)$ (Bradley and Harper 1988). When a uniform ion beam bombards a surface at incidence angle ϕ, its etching rate is

$$v(\phi, c_1, c_2) = (f/n)Y_0(\phi)[\cos\phi - \Gamma_1(\phi)c_1 - \Gamma_2(\phi)c_2] \tag{15}$$

where $Y_0(\phi)$ is the sputtering yield for a flat surface

$$Y_0(\phi) = \frac{p\varepsilon na}{\sqrt{2\pi}\sigma\mu}\exp\left(-\frac{a^2}{2\sigma^2}\right)B_1^{-1/2}(\phi)\exp\left(\frac{A^2(\phi)}{2B_1(\phi)}\right) \tag{16}$$

where f is the ion flux, n is the amount of atoms at unit volume in the amorphous solid, ϕ is the incidence angle, and p is the proportional constant relating the power deposited at the bombarded point to the rate of erosion. The other coefficients are defined as

$$\begin{aligned}
&c_1 = a\frac{\partial^2 h}{\partial x^2}(0), c_2 = a\frac{\partial^2 h}{\partial y^2}(0),\\
&A = \left(\frac{a}{\sigma}\right)^2 \sin\phi, B_1 = \left(\frac{a}{\sigma}\right)^2 \sin^2\phi + \left(\frac{a}{\mu}\right)^2 \cos^2\phi,\\
&B_2 = \left(\frac{a}{\sigma}\right)^2 \cos\phi, C = \frac{1}{2}\left[\left(\frac{a}{\mu}\right)^2 - \left(\frac{a}{\sigma}\right)^2\right]\sin\phi\cos\phi,\\
&\Gamma_1(\phi) = \frac{A}{B_1}\sin\phi - \frac{B_2}{2B_1}\left(1 + \frac{A^2}{B_1}\right)\cos\phi - \frac{AC}{B_1^2}\left(3 + \frac{A^2}{B_1}\right)\cos\phi,\\
&\Gamma_2(\phi) = -\frac{\mu^2}{a^2}\cos\phi\left(\frac{1}{2}B_2 + \frac{AC}{B_1}\right).
\end{aligned} \tag{17}$$

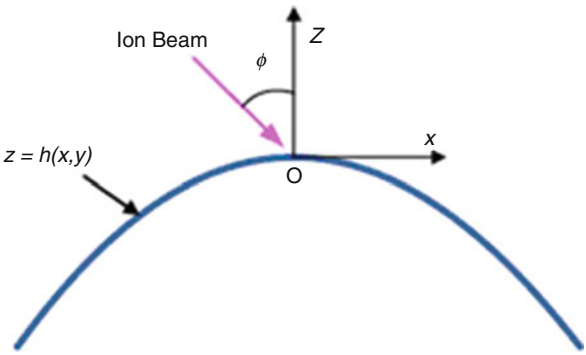

Fig. 8 Ions hitting an optical surface at the incidence angle ϕ

From Eq. 17, it can be seen that the coefficients c_1 and c_2 depend on the curvature of the surface and the coefficients $\Gamma_1(\phi)$, $\Gamma_2(\phi)$, and $Y_0(\phi)$ depend on the incident angle ϕ. Therefore, the relationship of etching rate function with incidence angle and bombarded surface curvature can be obtained using Eqs. 15–17.

Although Eq. 15 is the etching rate of uniform ion flux deduced in the micro area, it is also practicable in macro area with ion beam diameter in millimeter or centimeter scale since the local point flux could be considered identical. In Fig. 8, an ion beam with flux f bombards the surface at point O by the incidence angle ϕ; the distribution of flux is approximately $f(x\ \cos\ \phi,\ y)$ in workpiece reference frame (x, y, z) according to the projection theory. Thus the theoretical model of the beam removal function is

$$\mathrm{BRF}(\phi, c_1, c_2) = (1/n)Y_0(\phi)[\cos\phi - \Gamma_1(\phi)c_1 - \Gamma_2(\phi)c_2]f(x\cos\phi, y) \quad (18)$$

where c_1 and c_2 are

$$c_1 = a\frac{\partial^2 h}{\partial x^2}(0) = a/r_{0x}, c_2 = a\frac{\partial^2 h}{\partial y^2}(0) = a/r_{0y}.$$

For most of the surfaces (especially spherical surfaces), the unit of a is Å which is not comparable in magnitude with r_{0x} and r_{0y}. Hence c_1 and c_2 are infinitesimals, but $\Gamma_1(\phi)$ and $\Gamma_2(\phi)$ are finite coefficients, so Eq. 18 can be approximated by

$$\mathrm{BRF}(\phi, c_1, c_2) = (1/n)Y_0(\phi)\cos\phi f(x\cos\phi, y). \quad (19)$$

Equation 19 shows that the contribution of the curvature of surface to the beam removal function can be neglected. It can be concluded that the ion beam removal function varies with the varying of ion beam incidence angle and its footprint on the oxy plane transforms from circle to ellipse with the increasing of its incidence angle. In the following of this section simulation and experiment on the BRF will be done.

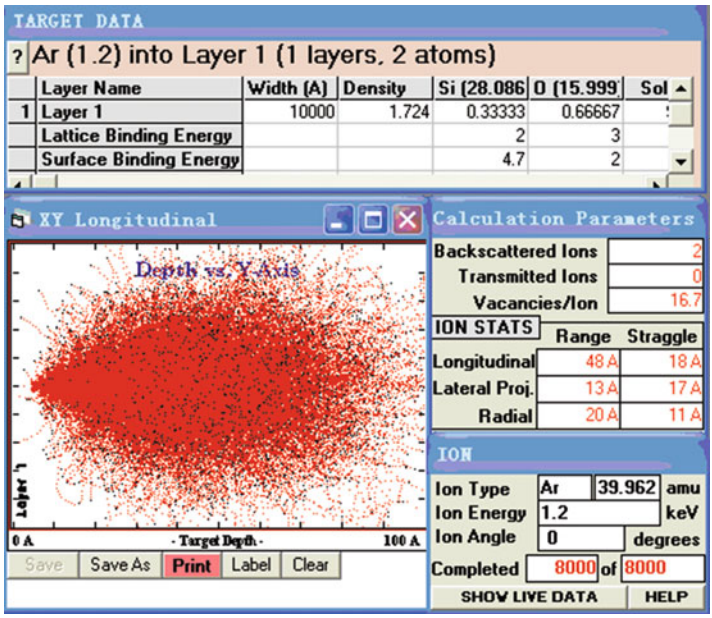

Fig. 9 The simulation result of Ar ions vertically incident on SiO_2

Assuming that 8,000 vertically incident Ar^+ with the energy of 1,200 eV were simulated to bombard fused silica by the SRIM program (http www srim org), then the parameters of ion energy distribution in Eq. 14 can be obtained. In Fig. 9, the simulation result shows that the average incidence depth of ions is $a = 48\ \mathring{A}$ and Gaussian distributing parameters are $\sigma = 20\ \mathring{A}$ and $\mu = 13\ \mathring{A}$.

From Eqs. 16 and 19, it is known that a theoretical beam removal function with arbitrary incident angle is difficult to be gained since the coefficients n, f and p in these equations are unobtainable. But a beam removal function with vertical incident angle is usually easily obtained by experiment. It is enlightened that to an arbitrary incident angle theoretical beam removal function, a valid way is to estimate it by that of vertical incident angle case which is unnecessarily known all above coefficients.

To gain a theoretical beam removal function model with arbitrary incident angle by this experimental method, the normalized peak etching rate is introduced:

$$k_\phi = \frac{p_\phi}{p_0} \tag{20}$$

where p_ϕ is the peak etching rate at incident angle ϕ and p_0 is the peak etching rate at vertical incident angle which can be estimated by experiment. Assuming that the ion beam is Gaussian distribution in figuring process, the beam removal function with arbitrary incident angle would be written as

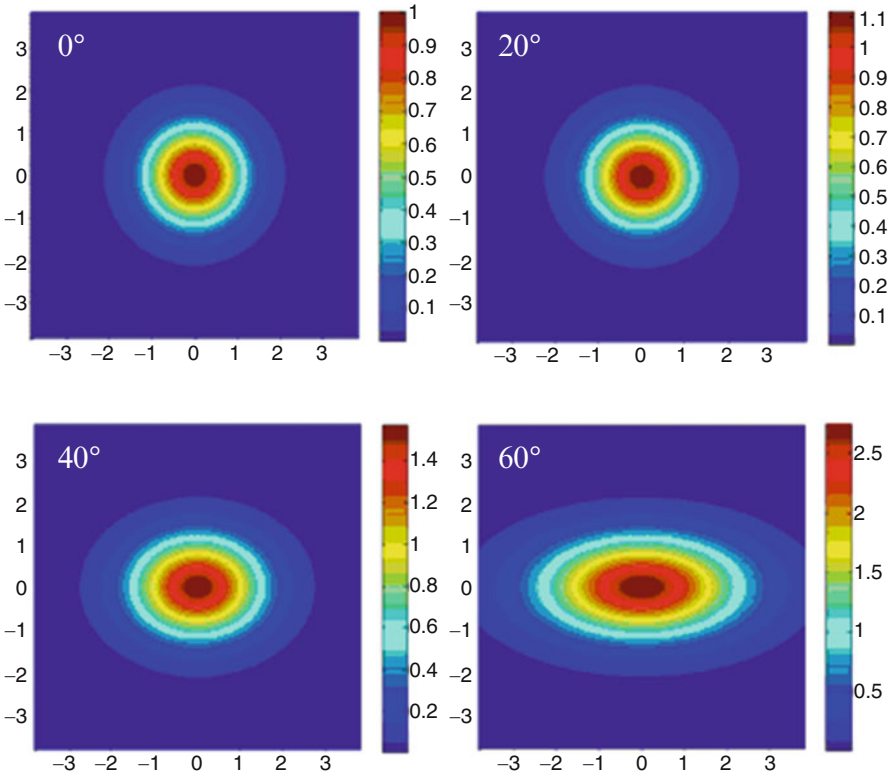

Fig. 10 The footprints of removal functions at different incidence angles

$$\mathrm{BRF}(\phi) = k_{\phi} p_0 \exp\left(-\frac{(x\cos\phi)^2 + y^2}{2\eta^2}\right). \tag{21}$$

Figure 10 shows the simulation result of the beam removal function with different incident angles with Eq. 21. It is apparently shown that the incident angle influences the footprint shape of the beam removal function, and their footprints on the oxy plane change from circle to ellipse and expanse their active zone with the increasing incident angles. However the length of semi-minor axis a is invariable, and the semi-major axis b is varying with $a/\cos\phi$.

Figure 11 also shows that the normalized peak etching rates depend strongly on the incident angle. It can be seen that the etching rate increases firstly and then decreases with the increasing incident angle. At about 70°, it reaches the maximum etching rate which is about 4.5 times than that at 0°.

To testify this theoretical model by experiment, an experimental equipment is set up in Fig. 12. In order to obtain removal functions with different incident angles, the experiment was done on six small fused silica samples (the size is 10 mm × 10 mm × 15 mm) with a 2 mm diameter ion beam. In this experiment,

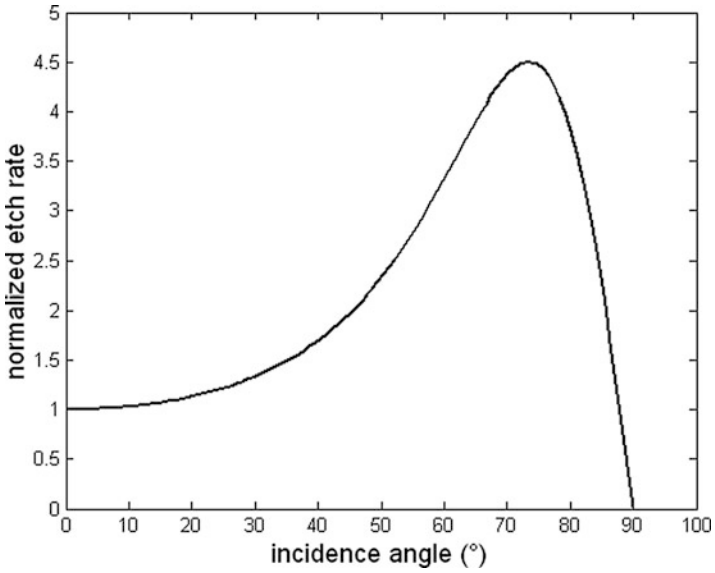

Fig. 11 The normalized peak etching rates vary with various incidence angles

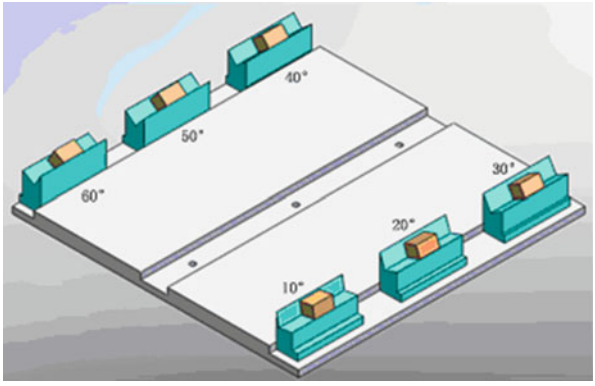

Fig. 12 The fixing method of the small fused silica samples

the samples are fixed at angles from 10° to 60° with 10° interval relative to the experimental planar board. The ion beam respectively bombards the surfaces of these samples along the vertical direction of experimental planar board. Every sample is bombarded 3 minuts, and the process parameters were set according to the modeling simulation. By this experiment, there are six footprints gained to estimate their beam removal functions. The one of footprints is shown in Fig. 13. All removal functions of this experiment are shown in Fig. 14, which validate the result of the theoretical analysis that the etching rates and footprints vary with incident angles.

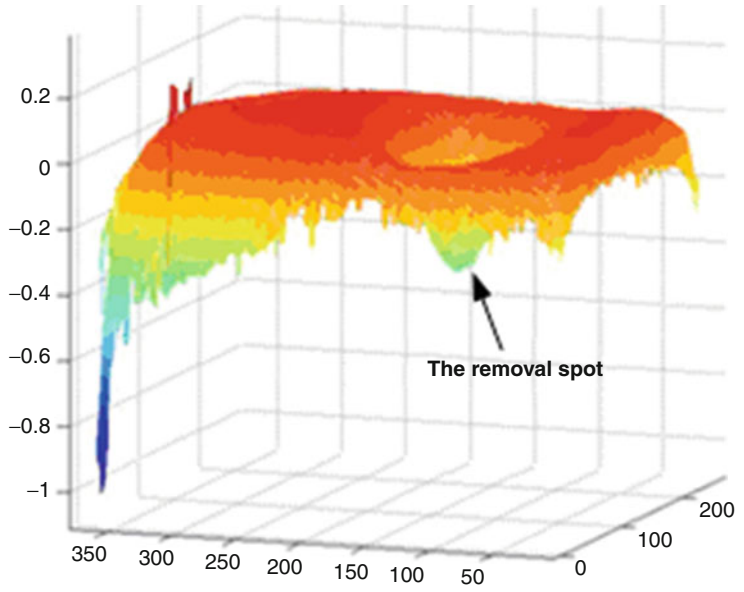

Fig. 13 The removal footprint on a fused silica sample

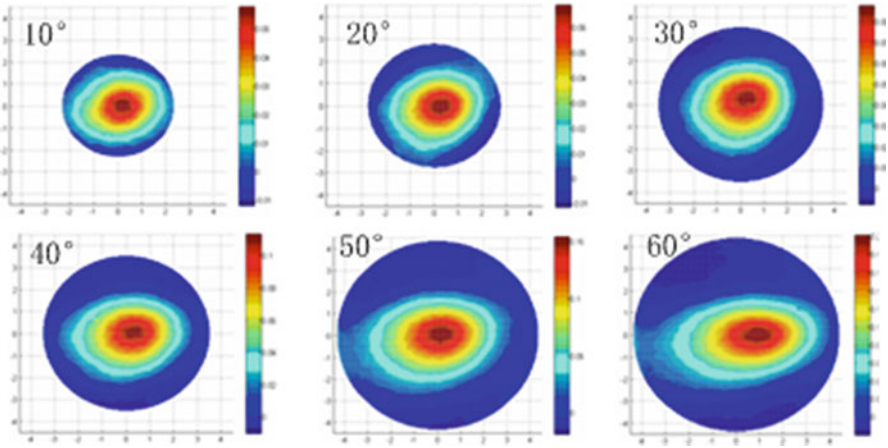

Fig. 14 Experimental removal functions depending on incidence angles

With Gauss–Newton method to fit these experimental beam removal functions, their beam removal functions are obtained as shown in Fig. 15. For example, the fitted model at 40° is shown in Fig. 16a, and its fitted residual error is acceptable (Fig. 16b). The footprint eigenvalues of these removal functions are estimated by 6σ method in mathematical statistics, which are shown in Fig. 17a with the semi-minor axis a and the semi-major axis b. In Fig. 17b, c, they show that

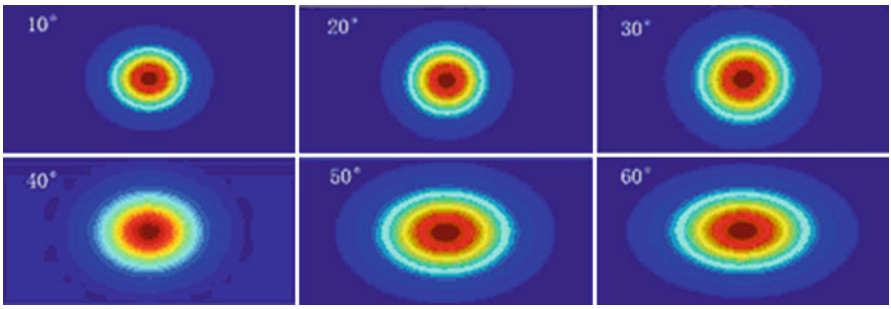

Fig. 15 The fitting result of the removal function

the eigenvalues and the etching rates of this experiment are close to the theoretical values. These results indicate that the length of semi-minor axis is approximately invariable and the semi-major axis is inversely proportional to the cosine of the incident angle.

From the above analysis, the following conclusions can be gained:

1. In IBF, the beam removal function varies with the ion beam incident angle.
2. To figure optical surface, the best way is that the ion beam bombards the surface along its normal direction, which can well constantly hold the etching rate and footprint of beam removal function.
3. For spherical and aspherical optical surface figuring, the good suggestion is that the ion source hold and motion mechanism is designed 5 axes motion mechanism to hold the ion beam moved along the normal direction of optical surface. For a 3-axis motion mechanism, the beam removal function must be real-time correct to compensate etching rate and footprint varying with the ion beam incident angle.

Contouring Algorithm for IBF

The figuring process is represented in Eq. 1. A significant step in the process is the calculation of dwell-time function that controls the correction of optical surface error. It is known that the ion beam figuring process is a convolution process and the calculation of dwell-time function is a deconvolution process.

To obtain good dwell-time function, there are three important problems that should be paid more attention which are (1) calculation algorithm, which calculates the dwell-time function distribution that will yield a desired material removal distribution when a specific beam removal function is applied; (2) the data process of optical surface edge, which influences the calculated dwell-time precision at the neighbor of surface edge; and (3) determining or predicting the optimal removed material amount or residual error result in every step of iteration, which is very important to gain the efficient dwell-time function and decrease the times of

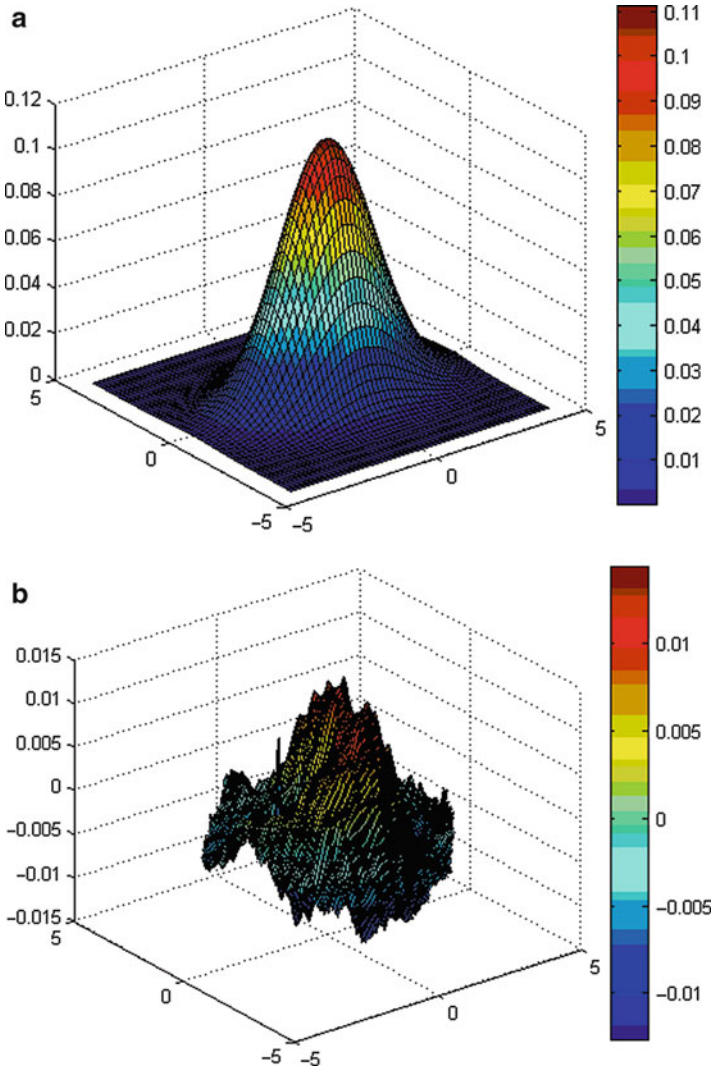

Fig. 16 The removal function at 40°corrected with Gauss–Newton fitting method

iteration and is very useful to control the middle- and high-spatial-frequency errors. About the third problem, it will be discussed in the next section.

About the algorithms to calculate the dwell time, they can be summed up to four kinds: (1) Fourier transform method (the early work was done by Wilson et al.) (1987); (2) iterative method for finding a solution to the dwell-time function (Allen and Roming 1990); (3) algebra method, such as wavelet algorithm (Shanbhag et al. 2000) and Bayesian algorithm (Changjun et al. 2009); and (4) matrix-based method, such as in Carnal et al. (1992) and Zhou lin et al. (2007).

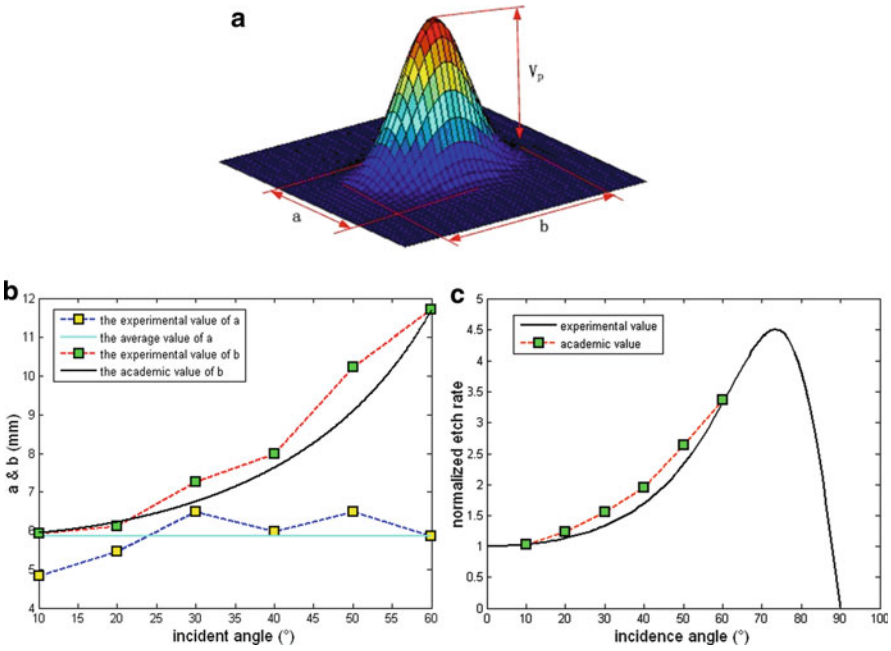

Fig. 17 The definition of the eigenvalues and the result of experiment: (**a**) the eigenvalues of the removal functions, (**b**) the changing rule of the footprint eigenvalues with various incidence angles, (**c**) the changing rule of etching rates with various incidence angles

Rewrite Eq. 1 as

$$R(x,y) = B(x,y) * T(x,y) = \int_{-\infty}^{\infty}\int_{-\infty}^{\infty} B(x-x', y-y')T(x',\, y')dx'dy'. \qquad (22)$$

Here, T is the dwell-time function. Assuming that the IBF scanning is a raster routine as shown in Fig. 2, there are two figuring techniques to realize the dwell time in the actual IBF: (1) position mode, where T represents the time that the ion beam spends at a location on the optical component per unit area, and (2) velocity mode, where T represents the ion beam raster scanning speed of a strip unit width.

In the position mode, the dwell-time function can either be broken into areas or interpreted as a time. So, the amount of removed material is proportional to the amount of time the ion beam must be positioned in the area which is equal to the integral of the dwell-time function over the area. For example, if the total optical component is broken into a square grid as shown in Fig. 18, the ion beam is centered at each square an mount of time approximately equal to the value of the dwell-time function at the center times the area of square, which discretizes Eq. 22 as

Fig. 18 The optical component broken into square grids

$$R(x,y) = \sum_{i=0} \sum_{j=0} B\left(x - x_i, y - y_j\right) T\left(x_i, y_j\right) \Delta x_i \Delta y_j. \tag{23}$$

This discretization of the removal function suggests that the figuring process can also be discretized in a similar way. Thereby the IBF process is represented as a discrete two-dimensional (2D) convolution. In actual figuring process, the optical component surface profile and the material removal function are provided as an x–y grid array from the profile interferometer, so the position mode process can be exactly realized with a square discrete convolution by maintaining the same discretization as the profile interferometer.

Alternatively, in the velocity mode, the optical component is broken in strips, where each strip has a width and a velocity function associated with it. The velocity function is the scanning speed that the ion beam moves along the strip and is equal to the inverse of the dwell-time function integrated over the strip width W:

$$V(x,y) = 1/\int_W T(x,y)ds. \tag{24}$$

Then Eq. 22 can be approximated as

$$R(x,y) = \sum_{i=0} \int_{-\infty}^{\infty} B\left(x - x', y - y_j\right) T\left(x', y_j\right) dx' \Delta y_j. \tag{25}$$

The IBF process is represented as a discrete one-dimensional (1D) convolution. Each one-dimensional strip has a raster interval. For example, if the optical component is broken into strips parallel to the x-axis, the raster interval width is Δy which is the y separation between the boundaries of the strips

$$V(x, y) = 1/T(x, y_i)\Delta y. \tag{26}$$

In this mode, the calculation of dwell time is more complicated than that of position mode since the precious material removed is related to the velocity and acceleration performance of the machine tool. This mode provides a partial discretization that has some advantages over the position mode. For the position mode, the ion beam remains on while it traverses from one grid point to another, which may cause unwanted material removed if the position time is not negligible compared to the dwell time in this grid area. In the velocity mode, the strip scanning is continuous which can avoid the unwanted material removed. In most cases, the velocity mode is chosen since the machine tool moves smoother which can decrease the generated middle or high-spatial-frequency error in the actual figuring process.

In the following of this section, an example is given about how to realize dwell time based on the Bayesian algorithm (Changjun et al. 2009).

Assuming that the optical surface error $E(x, y)$ and dwell-time function $T(x, y)$ are both random, the solution to dwell-time function $T(x, y)$ to maximize the posterior probability function P(T|E) of the dwell-time function according to the maximum likelihood method (Molina et al. 2001; Fang and Xiao 1998). With the Bayesian principle, the relation among the posterior probability function $P(T|E)$, the prior probability function $P(T)$, and the probability function $P(E|T)$ of the simulated removal error E if T were the true dwell time is

$$P(T|E) = P(E|T)P(T)/P(E). \tag{27}$$

In the IBF process, the ion beam density is the result of statistical average. Assume that it is of Poisson distribution and $P(E|T)$ follows the Poisson distribution with parameter $B \otimes T$. In this case, maximizing Eq. 27 could be transferred into the following minimization problem:

$$\min_T J_1(T) \tag{28}$$

where the performance function $J_1(T)$ is

$$J_1(T) = \iint_\Omega (B \otimes T - E\log(B \otimes T))\mathrm{d}x\mathrm{d}y. \tag{29}$$

With calculus of variation, the optimization condition for Eq. 28 can be deduced as

$$\frac{B(-x, -y)}{\iint_\Omega B\mathrm{d}x\mathrm{d}y} \otimes \frac{E}{B \otimes T} = 1. \tag{30}$$

With a multiplicative algorithm, the Bayesian-based iterative algorithm can be deduced from Eq. 30:

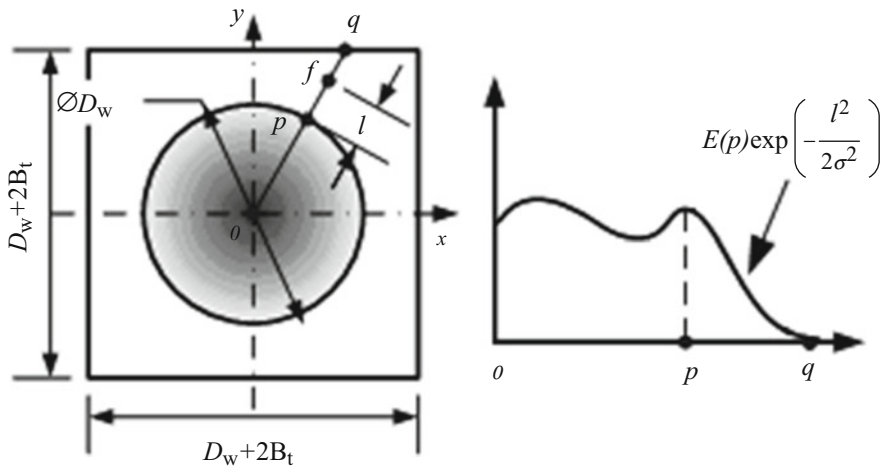

Fig. 19 Scheme of edge extension

$$T_{k+1} = T_k \times \left(\frac{B(-x, -y)}{\iint_{\Omega} B \mathrm{d}x\mathrm{d}y} \otimes \frac{E}{B \otimes T_k} \right). \tag{31}$$

Equation 31 is the generalized form of the traditional Richardson–Lucy algorithm (Lucy 1974; Richardson 1972) with respect to the nonnormalized removal function. This algorithm has an interesting property of nonnegativity: if the first estimate T_0 is nonnegative, none of the further estimate will be negative. In dwell-time iteration, the initial value is usually the offset nonnegative surface error. With this property, the nonnegativity demand of dwell time is satisfied.

In the beginning of this section, the data process of optical surface edge has been simply discussed. About how to solve this problem, it will be discussed. Since the optical shape usually is circular or non-regular, the discretized matrix of surface error function would not be filled completely, which may make the property of the points at the edge of the optical surface differ from that of the points in its inner. This difference can induce an algorithm edge effect which affects the convergence and calculated accuracy of algorithm at the edge of surface. So, it must be the edge extension which can weaken or even eliminate this effect. For example, in a circular optical component as shown in Fig. 19, the diameter of the component is D_w, and the radius of the removal function is B_t. The width of the extended rectangular area as shown in Fig. 19 is $(D_w + 2B_t)$. With a Gaussian algorithm, the data of any point f in the extended area of the surface error can be expressed as

$$E(\mathbf{f}) = E(\mathbf{p})\exp\left(-\frac{l^2}{2\sigma^2}\right) \tag{32}$$

where σ is the Gaussian extension parameter, generally $\sigma \geq Bt/3$. With the extended matrix above, only four fast Fourier transform computations are needed in one iteration of Bayesian-based algorithm in Eq. 31.

Analysis of Correcting Ability of IBF

In ion beam figuring, the ability to "correct" the surface errors of specific spatial wavelength or frequency depends on the ratio of the ion beam diameter d to the error wavelength λ, i.e., d/λ. The evalute of this correcting ability is the material removal efficiency ε, which is defined as the ratio of the volume of desired material removal to the volume of the predicted (or real) material removal. The Kodak had estimated that the ratio of the beam diameter to the error wavelength must be ≤ 0.5 to achieve 90 % of material removal efficiency (Allen and Keim 1989). It is obvious that the ion beam diameter is a key parameter in ion beam figuring process. In order to find an optimal ion beam diameter, Kodak used four ion beam diameters of 2.5, 5.1, 10.2, and 12.7 cm in their simulations to correct the presented error of wavelength of 10.5 and 9.5 cm. They found that the best choice is the 5.1 cm diameter which indicated an excellent correcting ability, while the total dwell time was favorable. Besides Kodak, the IOM in Germany also researched the correcting ability of different ion beam diameter. They used a smaller diameter down to 0.5 mm to meet the demanding requirements for correcting the long spatial wavelength part of the so-called mid-spatial-frequency roughness (MSFR) down to the sub-nanometer RMS level (Haensel et al. 2006). Further work has been done by Lin Zhou et al. in China (Lin et al. 2008, 2009). Assume that Eq. 25 is normalized as

$$R(x) = \int B(x - x')T(x')dx'. \tag{33}$$

And assume that the optical surface has the spatial frequency error R_λ

$$R_\lambda = \delta_\lambda \left(\sin\left(2\pi \frac{x}{\lambda}\right) + 1 \right) \tag{34}$$

where λ is the wavelength of the surface error and δ_λ is the amplitude of the error.

The circular Gaussian-shaped ion beam removal function is

$$B(x) = \frac{1}{\sqrt{2\pi}\sigma} e^{-\frac{x^2}{2\sigma^2}}. \tag{35}$$

Combining Eqs. 33–35, the dwell-time function can be calculated as

$$T(x) = \delta_\lambda \left[e^{2\left(\pi\frac{a}{\lambda}\right)^2} \left(\sin\left(2\pi \frac{x}{\lambda}\right) + 1 \right) \right]. \tag{36}$$

Since the dwell-time function distribution must be nonnegative, the actual dwell-time function distribution is

$$T_a(x) = T(x) - \inf[T(x)] = \delta_\lambda e^{2\left(\pi\frac{a}{\lambda}\right)^2} \sin\left(2\pi\frac{x}{\lambda}\right) + \delta_\lambda e^{2\left(\pi\frac{a}{\lambda}\right)^2}. \tag{37}$$

Based on Eqs. 33 and 37, the actual material removed can be calculated as

$$R_a(x) = R_\lambda + \delta_\lambda\left(e^{2\left(\pi\frac{a}{\lambda}\right)^2} - 1\right). \tag{38}$$

Equation 38 shows that in any ion beam figuring process, there are always extra materials removed. The extra removal material $\gamma(x)$ is

$$\gamma(x) = R_a(x) - R_\lambda(x) = \delta_\lambda\left(e^{2\left(\frac{\pi}{6}\frac{d}{\lambda}\right)^2} - 1\right) \tag{39}$$

where $d = 6\sigma$ is the ion beam diameter. Equation 39 shows that the extra removal material $\gamma(x)$ is independent of x; therefore, $\gamma(x)$ can be shortly written as γ.

The material removal efficiency ε can be described as

$$\varepsilon = \frac{\delta_\lambda}{\delta_\lambda + \gamma} = e^{-\frac{\pi^2}{18}\left(\frac{d}{\lambda}\right)^2}. \tag{40}$$

Equation 40 shows that the material removal efficiency ε is a negative exponential function of d/λ. For a known spatial frequency error with wavelength λ, the more the beam diameter is, the less the material removal efficiency. For a given beam diameter, the smaller the wavelength is, the less the material removal efficiency. In this sense, the smaller ion beam diameter is always a best choice in ion beam figuring. However smaller ion beam diameter always result in more process time, which usually decreases the process reliability. To balance the material removal efficiency and process stability, a suitable ion beam diameter should be chosen.

Simulating the material removal efficiency ε at different conditions of d/λ and comparing the results with the theoretical results achieved by Eq. 40, based on the result shown in Fig. 20, it can be seen that the simulation-predicted material removal efficiencies are in satisfactory agreement with the theoretical ones. From Fig. 20, it can be seen that the material removal efficiency is 87 % when d/λ is 0.5. This value approximately corresponds to the Allen's estimated material removal efficiency, 90 % (Allen and Keim 1989), which is acceptable in ion beam figuring process. When the ratio of d/λ is up to 1, the ε rapidly decreases to 58 % which is unacceptable, and it extremely degrades to only 11 % when the ratio is up to 2.

According to theoretical analysis and simulation results, it is recommended that the ratio of d/λ should be less than 0.5 in order to obtain acceptable material removal efficiency in ion beam figuring process.

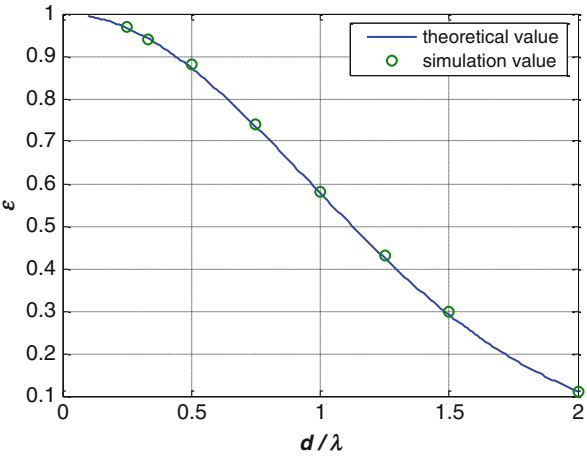

Fig. 20 Comparison of theoretical material removal efficiencies with the simulation ones

The Optimum Material Removal of IBF

It has been known that if the less desired material removal is specified, the calculated dwell function is consequently small for a given initial surface figure error, which means a short IBF process time, but as a result, the actual post-machined residual surface figure error is great. If a larger desired material removal is specified, although the resulted residual figure error is smaller, the calculated dwell function is greater, which means a longer process time.

Therefore, in order to balance the process time, which is determined by the dwell function and the resulted residual error, the desired material removal specified to the contour algorithms should be considered and optimized. In this section, it will be discussed how to determine an optimum material removal. Firstly the conventional method to determine the removal is discussed in Lin Zhou et al. (2010).

Since the real removal in an IBF process is always nonnegative, the specified removal should be nonnegative too. However, the data of a surface figure error from metrology usually contain negative elements. Therefore, in order to obtain a nonnegative removal, the conventional method is that the error data is simply offset to be nonnegative:

$$\boldsymbol{R} = \boldsymbol{E} - \min(\boldsymbol{E}) \tag{41}$$

where R is the desired material removal and E is the surface figure error and $\min(\boldsymbol{E})$ is the minimum of E. This method is illustrated in Fig. 21. Due to the original surface figure error from metrology that inevitably contains noises, E should be smoothed to reduce the influence of noises on the magnitude of $\min(\boldsymbol{E})$. With a smoothed figure error, the removal determined by Eq. 41 is reasonable.

However, for ultraprecision optics, in order to keep more details or higher-spatial-frequency information about the figure error, the original figure error from metrology is often used instead of the smoothed figure error. For original errors,

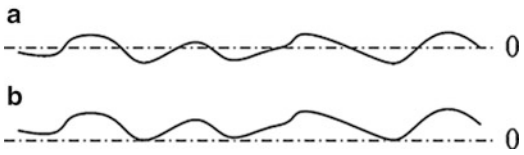

Fig. 21 Illustration of conventional method to determine specified removal. (**a**) Error profile from metrology; (**b**) determined specified removal R ($R \geq 0$)

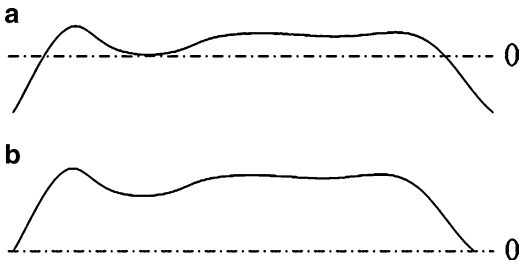

Fig. 22 Calculated result of error profile with edge fall. (**a**) Error profile from metrology; (**b**) determined specified removal R ($R \geq 0$)

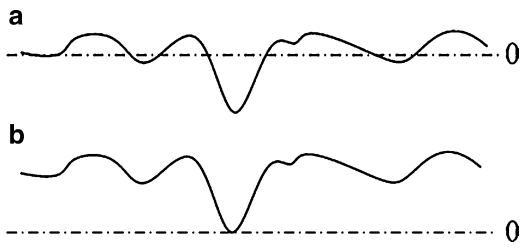

Fig. 23 Calculated result of error profile with pits. (**a**) Error profile from metrology; (**b**) determined specified removal R ($R \geq 0$)

since they contain more noises, and more edge fall and pits, as shown in Figs. 22 and 23, the material removal determined by Eq. 41 are not reasonable and tend to be greater, consequently causing longer IBF process time.

It is concluded that, in the conventional method, the material removal is the sum of the figure error and an invariable uniform material removal. To avoid the drawback of the conventional method, Lin Zhou et al. proposed an optimum material removal method which determines the material removal flexibly (Lin Zhou et al. 2010). In this method, an adjustable uniform removal U is introduced to substitute the invariable $[-\min(\boldsymbol{E})]$. The formula is

$$\boldsymbol{R} = \begin{cases} \boldsymbol{E} + U, & \boldsymbol{E} + U \geq 0 \\ 0, & \boldsymbol{E} + U < 0 \end{cases}. \tag{42}$$

In Eq. 42, the adjustable uniform removal U can be broken into two parts, i.e., $U = \gamma e$, where e is the RMS value of the figure error E and γ is an adjustable parameter to be used to control the magnitude of the material removal. Since e describes the mean deviations of the figure error, it contains the main information

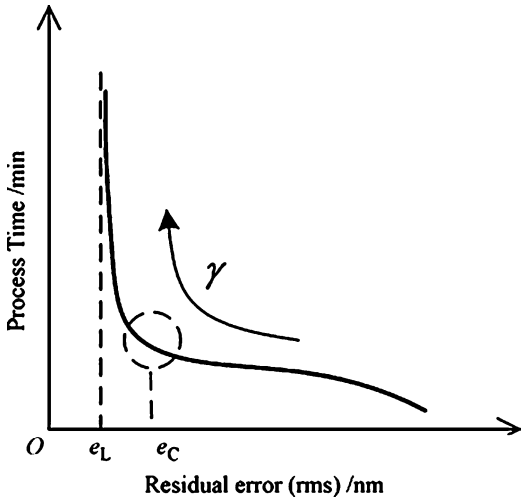

Fig. 24 Typical figure-prediction curve (process time vs. RMS value of residual figure error)

of the figure error. Therefore, the adjustable parameter γ is just a simple factor, and for different figure error, the optimum γ values experientially tend to be in the same range from 1 to 4.

Since the iterative dwell-time function algorithm is simple and has met with considerable success in practice, this problem is discussed by one iterative algorithm expressed as (Drueding et al. 1995)

$$\boldsymbol{T}_{n+1} = \boldsymbol{T}_n + \xi \boldsymbol{E}_n, \quad \boldsymbol{E}_n = \boldsymbol{R} - \boldsymbol{B} * \boldsymbol{T}_n \tag{43}$$

where T_n and E_n are the dwell time and the residual figure error after n computation iterations, respectively, ξ is the relaxation factor, and B is the beam removal function. The initial T_0 is often set to a proportion of the specified removal, usually $T_0 = R/B_0$, where B_0 is the integration of B. After several computation iterations, the final dwell time and the residual error can be obtained.

For different γ value, the material removal is differently determined by Eq. 42, and consequently the results, which are calculated in Eq. 43, including dwell time and residual figure error, are different too.

A γ curve in a coordinate system of process time (the sum of all dwell time, total dwell time) vs. RMS value of the residual error is shown in Fig. 24, which is called a figuring prediction curve which is usually a monotonically decreasing curve. In this curve, it can be seen that a larger material removal causes a smaller residual error, but consumes a longer process time, and a smaller material removal causes a shorter process time, but induce a larger residual error. This implies it is difficult to determine an optimum material removal for both small residual figure error and

short process time. However, fortunately, a figuring prediction curve is often in the shape of the letter "L." This property is useful to determine the optimum material removal. The optimum material removal should be located at the corner of the letter "L," since for removals smaller than this point, the residual error decreases rapidly while the process time increases slowly and, for removals greater than this point, the process time increases rapidly without much decrease in residual error.

In addition, the figuring prediction curve can be used to predict the process time and the residual figure error of an IBF process. Since the figuring prediction curve is in the shape of the letter "L," there exist two significant RMS, the corner's RMS e_C and the smallest RMS e_L; both are illustrated in Fig. 24. For an initial optical surface, if the desired residual error is represented by e_D RMS, then an IBF process can be classified into one of the following three cases according to the magnitude of e_D:

1. $e_D < e_L$
   In this case, the figuring prediction curve indicates that the desired accuracy cannot be obtained. This implies that the initial figure error is too great to be removed. Therefore the optical component should be returned to the prepolishing process for a smaller initial error.
2. $e_L < e_D < e_C$
   In this case, although the figure-prediction curve indicates that the desired accuracy can be obtained, the process time is too long to be practicable. Therefore, the optical component should also be returned to the prepolishing process for a smaller initial error.
3. $e_D > e_C$
   In this case, the figuring prediction curve indicates that the desired accuracy can be obtained in a practicable process time and the optimum removal at the corner is preferred. Moreover, in this case, if the desired RMS e_D is significantly greater than the corner's RMS e_C, to reduce the process time, a smaller removal may be chosen instead of the corner's removal.

Although the property of the "L" shape about the figure-prediction curve is found out in the iterative contour algorithm, it also exists in other contour algorithms, such as the matrix algebraic algorithm. Therefore, this method to determine the optimum material removal can be used in other contour algorithms.

A suggestion should be given that a smaller material removal is advisable. According to simulations, a process with larger removal usually induces a smaller residual figure error. However, in a real process, the resulted residual figure error from a process with larger removal is often significantly greater than the prediction. In addition, some experiments have indicated that a process with more removal will likely degrade surface roughness. Therefore, for an IBF process, a smaller material removal is advisable.

Realization of IBF Technique

This section describes the operational steps to realize IBF technique. The procedure used in the process is outlined below:

1. Calculating the removal map
   At the beginning of process, an interferometric map of the optical component's surface height data (or called surface map) is loaded in an array. For aspherical optical surface, this surface map should be calibrated according to the curvature of aspherical surface since the distortion of measure data project. The removal map is equal to the surface map minus the component's desired surface map. This removal map generally needs to be filtered by Zernike polynomial to avoid influence of the measure noise or high-spatial-frequency error. With this way, it makes the IBF machine move smoothly. Further work in this step is the removal map data extension along the component edge.
2. Selecting beam removal function
   It is the most important step to select a suitable beam removal function in an IBF process. It has been known that there are two key parameters for a Gaussian beam removal function, which are beam diameter d evaluated by the full width at half maximum (FWHM) or 6σ and the peak material removal rate (or volume removal rate), which is mainly controlled by the ion beam voltage and current. About how to gain a suitable beam diameter, it will be discussed below.

There are two methods to change the diameter of ion beam. The direct method is to decrease the scale of screen grid of the ion source shown in Fig. 25a. By this way, there is a ratio between the diameter of screen grid and the diameter of ion source inner chamber. This ratio is about 1:4. For example, in a 90 mm ion source, the minimal diameter of screen grid is about 22.5 mm. Based on the ratio, the better practical selectable range of screen grid is 25–90 mm for 90 mm ion source, 15–50 mm for 50 mm ion source, 10–30 mm for 30 mm ion source, and so on. In these ranges, it can gain satisfied material removal rate universally. Otherwise, its peak material removal rate and volume material removal rate are rapidly reduced as the diameter of ion beam decreases. For example, when the diameter of ion beam decreases from 25 mm to 15 mm for 90 mm ion source, its peak material removal rate is rapidly reduced from 0.13 μm/min to 0.025 μm/min, and its volume material removal rate is also reduced from 16.6×10^3 mm^{-3}/min to 1.67×10^{-3} mm^3/min from 0.13 μm/min to 0.025 μm/min (Xie Xuhui et al. 2009). Because the material removal rate decreases rapidly as the diameter of screen grid decreases, it is difficult to gain very small ion beam by this method. Currently, with this method, the smallest stable ion beam is about 4–5 mm(FWHM) by 3 cm ion beam in IBF. To gain more small ion beam, another method is to put an ion diaphragm (or mask) before the ion beam outlet of the ion source which passes only part of the ion beam through the ion diaphragm as shown in Fig. 25b. Compared with the direct method,

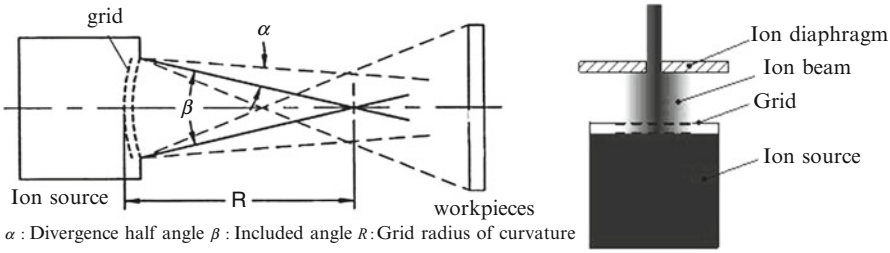

Fig. 25 The methods to gain the suitable diameter of ion beam

this method is a secondary way which can gain about 0.5–4 mm Gaussian-type ion beam (FWHM) with good peak material removal rate. For example, by this way, it is able to gain 1.7 mm diameter (FWHM) of ion beam with a 2 mm diameter of ion diaphragm with peak material removal rate about 200 nm/min (5 cm ion source with 40 mA ion beam current, 1,000 eV ion beam voltage). And the ion beam longtime stability is better than 2 %/3 h. So, it is a conclusion that ion diaphragm is an efficient method to gain more small ion beam which has a good performance to improve IBF figuring ability. Said to this, there is a problem would be paid attention that a match relationship between the diameter of screen grid and the diameter of ion diaphragm is also existed to get full Gaussian-type material removal function.

Based on the above discussion, the following conclusions can be drawn:

1. Different beam removal function can be gained by selecting suitable screen grid and ion beam power parameters.
2. Ion diaphragm is a good secondary method to improve IBF figuring ability.
3. In IBF process, it would select different screen grid and ion diaphragm to control full spatial frequency figuring error.

3. Calculating and Realizing the dwell-time function

About how to calculate dwell-time function, it is has been discussed in detail in the above section. Here, it is discussed how to realize the dwell time which may be seen in the continuation of the section "Contouring Algorithm for IBF."

Continuing the Bayesian-based algorithm discussion in the section "The Typical Features and Its Purpose of IBF," assuming that the desired dwell-time function is $T(x, y)$, the discrete intervals are Sx, Sy along the x and y direction, respectively. In the figuring process, the ion beam scans continuously in the x direction and raster moves in the y direction. Omitting the transient (acceleration and deceleration) of the translation system, the velocity distribution in the x direction can be computed as

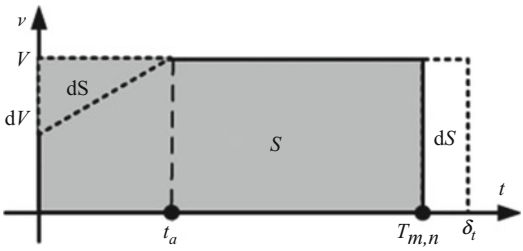

Fig. 26 Diagram for analysis of realization error with approximated velocity

$$V = \frac{S_x}{T(x,y)S_xS_y} = \frac{1}{T(x,y)S_y}. \tag{44}$$

The variation of the dwell time along the x direction introduces the transient and induces a realization error of dwell time with velocity given by Eq. 44. As shown in Fig. 26, the relative realization error of dwell time is

$$\varepsilon = \frac{\delta_t}{TS_xS_y} = \frac{(\mathrm{d}T_{S_x}(x,y))^2}{2aT^4(x,y)S_xS_y^2} = \frac{S_x(\partial_x T)^2}{2aT^4S_y^2} \tag{45}$$

where a is the acceleration of the translation system. Equation 45 indicates that the relative realization error is inversely proportional to the acceleration a and to the square of intermittent increment S_y^2 and is proportional to $(\partial_x T)^2$.

Smoothing Eq. 45, it indicates that it can reduce the realization error. In order to smooth dwell time and to de-noise, total variation norm $J_2(T)$ is introduced, which is gradient based:

$$J_2(T) = \mu \iint_{\Omega} |\nabla T| \mathrm{d}x\mathrm{d}y \tag{46}$$

where μ is a weight factor. Adding Eq. 29 to Eq. 46, then the minimization problem is transferred as

$$\min_T (J_1 + J_2). \tag{47}$$

With calculus of variation and multiplicative algorithm, the modified Bayesian-based algorithm for dwell time can be deduced as

$$T_{k+1} = \frac{T_k}{1 - \mu \frac{\Delta T_k}{|\nabla T_k|}} \times \left(\frac{R(-x, -y)}{\iint_{\Omega} R\mathrm{d}x\mathrm{d}y} \otimes \frac{E}{R \otimes T} \right) = \varphi'(T_k). \tag{48}$$

In the iterative process with Eq. 48, a small weight factor μ cannot smooth the dwell time and cannot filter the noise. On the other hand, a large eight factor can

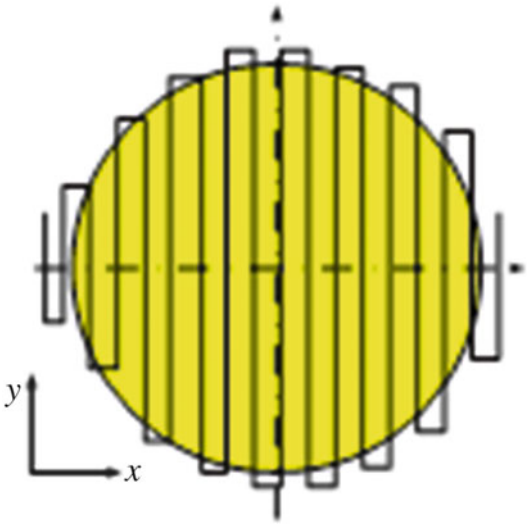

Fig. 27 The raster scanning of IBF

make dwell time so smooth as to reduce the precision of dwell-time density function. There is a trade-off.

Another key problem in the calculation of dwell time is the raster pitch (interval). In the raster scanning of ion beam figuring as shown in Fig. 27, the x direction is the scanning direction and the y direction is the raster direction. In the actual figuring process, the "tool trace" can be seen as raster pitch increasing as shown in Fig. 28, which will generate the middle- or high-spatial-frequency residual surface errors on the optical surface. In Fig. 28, the ion beam removal function has 5 mm diameter.

How is a suitable raster pitch to control its figuring residual errors selected? Answering this question, the figuring precision and its efficiency (or figuring time) are needed in actual process firstly. According to the Nyquist sample theorem, the pitch spatial frequency should be at least twice larger than the spatial cutoff frequency of the removal function. Assuming the axial symmetric removal Gaussian function has W width (6σ), its cutoff frequency will be

$$f_c = \frac{9}{\pi W}. \tag{49}$$

So the raster pitch should satisfy

$$T_s < \frac{1}{2f_c} = \frac{\pi W}{18}. \tag{50}$$

As known in Eq. 49, the small ion beam needs small pitch to satisfy the sample theorem. But in the actual process, an optimized pitch should be considered to match the precision and efficiency comprehensively. By computer simulation of the

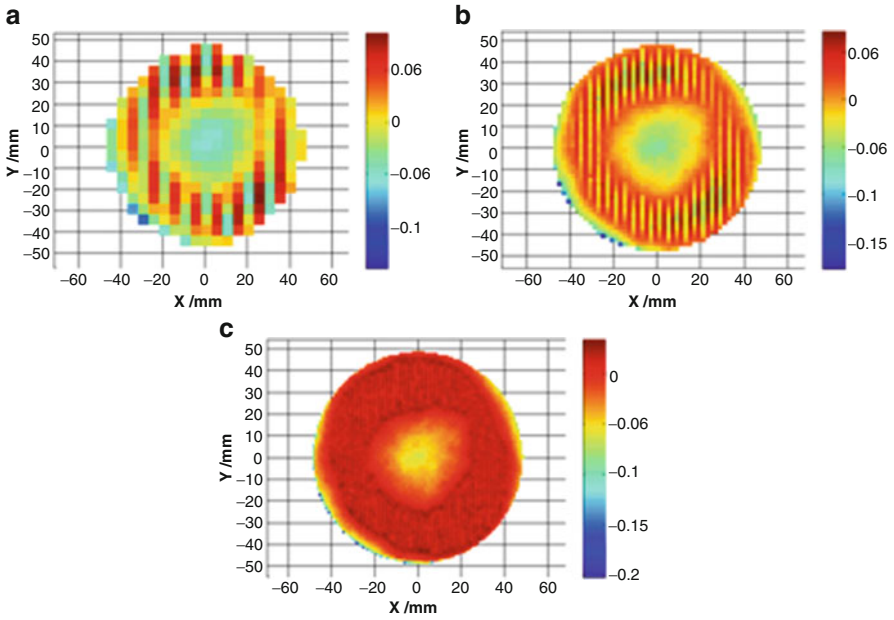

Fig. 28 Simulated residual machining errors for different raster pitches. (**a**) 5 mm raster pitch. (**b**) 2 mm raster pitch. (**c**) 1 mm raster pitch

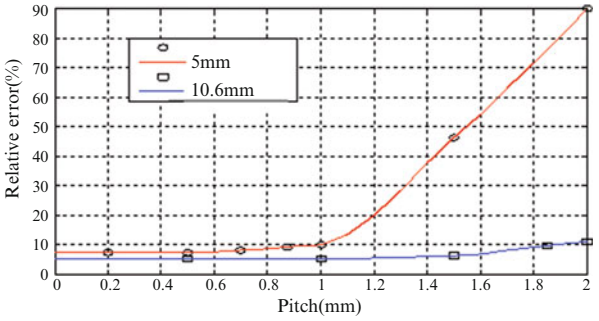

Fig. 29 Simulation of pitch vs. its machining error for ϕ100 mm planar optics

pitches and its related figuring errors from small to large pitches, a curve of the pitch vs. its figuring error can be drawn. An example shown in Fig. 29, the "dot" curve is for 5 mm diameter of ion beam and "square" one is for 10.6 mm diameter of ion beam. It can be seen that each curve has one turning point – 1 mm pitch for 5 mm diameter of ion beam and 1.8 mm pitch for 10.6 mm diameter of ion beam, respectively. The turning point means that the change of relative figuring error (the ratio of actual figuring error to its desired error) is slower below this point, while faster above it. For example, of the "dot" curve in Fig. 29, when the pitches are smaller than 1 mm, their relative figuring errors are smaller than 10 %. When they

are larger than 1 mm, their relative figuring errors are increased rapidly. So the result that the 1 mm pitch would be selected as the raster pitch for 5 mm diameter of ion beam is obtained, which makes good trade-off between the relative figuring error and the figuring efficiency. With the above analysis, it is known that a curve of pitch vs. its figuring error can be set up to help in selecting the optimal pitch (Xuhui et al. 2011).

The Challenges of IBF Technical Development

High-Gradient Optical Surface Figuring by IBF

In the above section, the measure data project distortion has been discussed. For high-gradient optical surface, this problem must be considered seriously when the surface error $E(x, y, z)$ is projected from three-dimensional (3D) Cartesian frame to 2D frame, resulting in $E(x, y)$ for the deconvolution operation. Furthermore, in order to maintain a constant removal function at every dwell point, the ion beam is usually held perpendicular to the surfaces. This means at least five axes and larger workspace is required. If wanting to figure high-slope surfaces with a linear three-axis machine, which is definitely economical and more reliable compared with a five-axis system, some problems should be solved first. Thomas Haensel et al. (2008) and Dai Yifan et al. (2010) have discussed to figure strongly curved surfaces with a linear three-axis system in IBF.

In the section "Removal Function Modeling and Analyzing of IBF," the changing rule of the removal function has been discussed with the incident angle based on theoretical and experimental investigation of the removal characteristics, which is used to figure high-gradient optical surface.

As shown in Fig. 30, a Gaussian ion beam bombards a high-slope surface $z' = h(x', y')$ parallel to the optical axis. The actual removal rate at point $B'(x', y')$ in the action region is $R_{\theta ij}$ when the beam dwells at point $A'(x', y')$ with a removal function $R(x, y)$. Since the dwell time is calculated in 2D plane (OXY), the nominal removal rate at $B(x, y)$ is R_{ij}, which is obviously unequal to the nominal one $R_{\theta ij}$. The normalized removal rate is

$$K_{ij} = \frac{R_{\theta ij}}{R_{ij}} \tag{51}$$

where θ is the incident angle. $R_{\theta ij}$ and R_{ij} are defined as

$$R_{\theta ij} = R_\theta\left(x' - x_i', y' - y_j'\right) R_{ij} = R\left(x' - x_i', y' - y_j'\right).$$

So the actual removal rate becomes $R_{\theta ij} = K_{ij} R_{ij}$. By compensating the change of coefficient K_{ij}, according to the removal characteristics in IBF process, the original program developed for figuring flat surfaces is still applicable to high-slope surfaces.

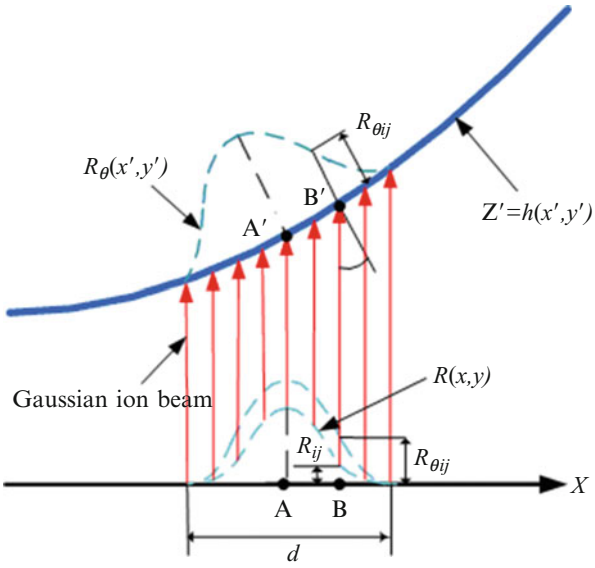

Fig. 30 Ion beam figuring of a high-slope surface along the optical axis

Substituting the normalized removal rate K_{ij} into Eq. 19, which is the theoretical model of the removal function, it can be seen that the function at arbitrary incident angle can be gained when the removal function with perpendicular incident is obtained through experiments:

$$R(x, y) = K_\theta R_0 f(x \cos\theta, y). \tag{52}$$

Based on Eq. 52, the curve of normalized peak removal rate is shown in Fig. 31 with the energy dispersion parameters determined. It can be verified through experiments with the ion beam scanning linearly and etching a sample along one of its generatrix. For example, the target distance is fixed and the constant scanning velocity is 1 mm/min. The aperture of the target surface is 21.3 mm, and the radius of curvature is 16 mm, which indicates the maximal incident angle is 41.7°. The actual material removal is shown in Fig. 32. For the purpose of comparison, the experimental curve of the removal rate is drawn in Fig. 31. It is consistent with the theoretical curve. Therefore it is reasonable to apply the theoretical model instead of a series of experiments to get the removal rate for high-slope samples of various apertures and various curvatures (Dai et al. 2010). A figuring experiment is done to testify this method with 5.7 mm (6σ) diameter ion beam on a linear three-axis IBF machine.

Figure 33a shows the original surface error map before figuring (101.9 nm PV and 13.1 nm RMS). According to the theoretical analysis and experiment, the distribution of the normalized removal rate K_{ij} is given in Fig. 33b.

The first iteration aims to confirm the positioning precision and remove surface protuberances. It takes 4.2 min to reduce the figure error to 99.8 nm PV and 8.5 nm RMS with RMS convergence ratio 1.55. The residual error map shown in Fig. 34a

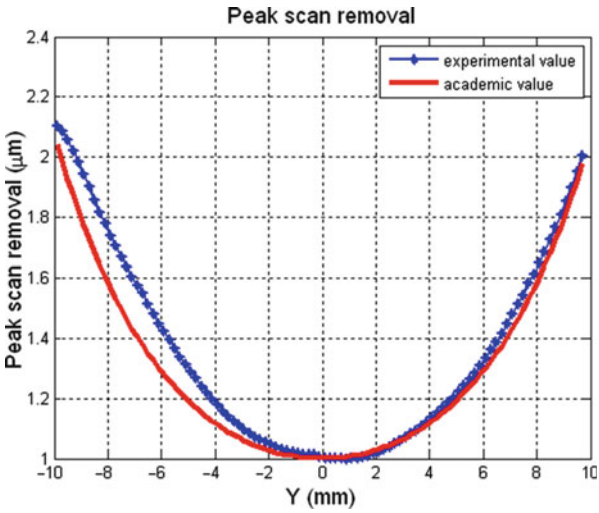

Fig. 31 Theoretical and experimental curves of the removal rate

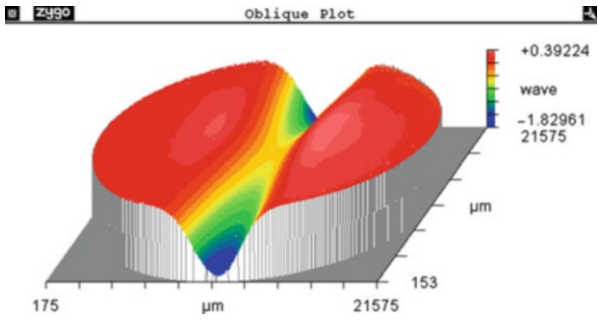

Fig. 32 The removal result by linearly scanning a spherical surface

indicates that the local protuberances at central and marginal regions have been removed, and the RMS error is reduced evidently. In this iteration, the ion beam positioning problem is met. Xuhui et al. (2011) have discussed how to solve it. Then in the next iteration, it takes only 4.8 min to reduce the figure error to 44.3 nm PV and 5.9 nm RMS, with RMS convergence ratio 1.44, comparable to that in flat surface figuring. The final figure error map is shown in Fig. 34b.

The total time consumed is 9 min, and the total convergence ratio reaches 2.24. Moreover, the figure error at the marginal region is successfully corrected without edge effect. This experiment proves the proposed method is excellent for figuring of high-slope surfaces.

Based on figure error compensation, the influence of varying removal function and projection distortion on the dwell-time solution is reduced when figuring a high-slope surface. Hence the five-axis figuring machine can be replaced by a three-axis one with smaller workspace. And the program for figuring flat surfaces still works in high-slope cases. The limitation is that the maximal incident angle is

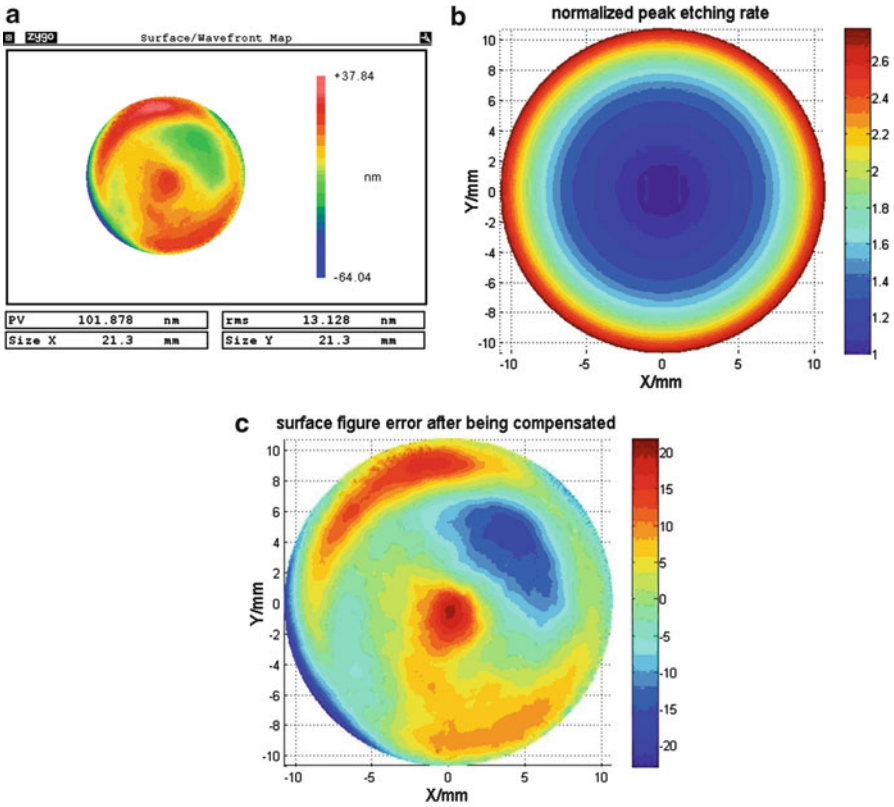

Fig. 33 The surface error. (**a**) The original figure error. (**b**) The distribution of normalized peak removal rate. (**c**) The compensated figure error

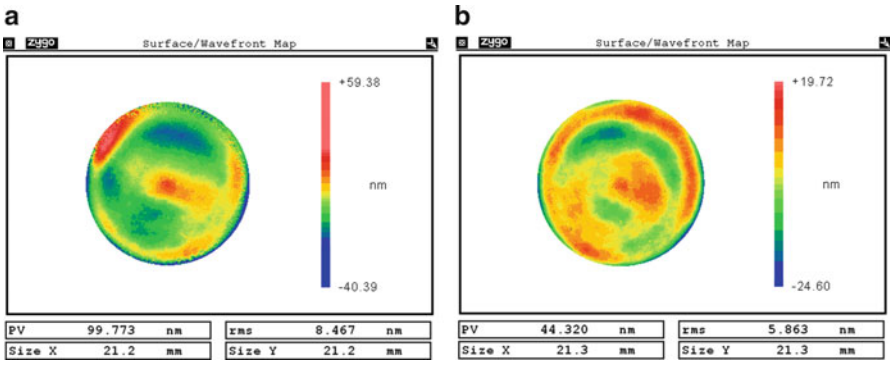

Fig. 34 The figuring results of a high-slope optical surface. (**a**) Figure error after the first iteration. (**b**) Figure error after the second iteration

required within about 60°. For higher-slope surfaces, the uniform gridding partition of surface error in 2D plane would lead to loss of local details including some high-frequency errors. To solve this problem, it will be with a smaller ion beam and subregion stitching method.

High Thermal Expansion and Crystal Optics Figuring by IBF

Unlike conventional methods, ion beam figuring process must be in the vacuum environment and generates high surface temperature on optical component because some part of the energy which is not transferred to component atom momentum heats the component. This section mainly talks about the thermal effects on optical component in the IBF process.

To know the temperature effect, the direct method is to measure the surface temperature by thermo-sensor, such as thermocouples, infrared camera, etc. (Gailly et al. 1999; Xuhui et al. 2012). The aim to discuss the temperature effect is to solve its influence to the optical component, especially to the high thermal expansion and crystal optics. The better method to solve this problem is to construct a thermal model to estimate the surface temperature (Xuhui et al. 2012; Nelson 2010).

For the thermal modeling of component, something should be known about the ion beam, such as ion beam power density distribution, ion beam power reached to component, absorbed energy (heat) by component, and so on. Only known to these problems, a useful thermal model may be set up to correctly estimate the component temperature and its distribution.

In ion beam, ion (A_r+) proportion is about 75–90 %; the other 25–10 % is the neutron-atom. When the ion beam runs from the outlet of ion source to the surface of component, its power will be lose partly because of resonance charge exchanging between the ions and neutron-atoms. So, the ion beam power P' that reached to the surface of the component is

$$P' = \eta IU = \eta P \tag{53}$$

where I is the ion beam electro-current, U is its voltage, P is the ion beam power generated by ion source, and η is the correcting factor of ion beam. Based on the ion beam correcting theory (Meinel et al. 1965), this correcting factor mainly lies on the section area of resonance charge exchange and ion velocity

$$\eta = \exp\left(-\frac{kTd}{\sqrt{2}P_0\sigma_{\mathrm{RCE}}}\right) \tag{54}$$

where e, E_i, and M_i are the ion charge, ion energy, and ion mass, respectively; a and b are the ion constants; k is the Boltzmann constant; P_0 is the pressure of vacuum; d is the distance of ion source outlet to the surface of component; and σ_{RCE} is the section of resonance charge exchange:

$$\sigma_{\mathrm{RCE}} = \left(a - b\ln\left(\sqrt{\frac{2eE_i}{M_i}}b\right)\right). \tag{55}$$

The ion velocity is

$$v_b = \sqrt{\frac{2eE_i}{M_i}}. \tag{56}$$

Therefore, the ion beam power P' that reached to the surface of component can be gained theoretically by Eqs. 53–56.

The power that reached to the surface component is divided into two parts. One is so-called sputter power which is transferred to component atom momentum to make the atom escape the surface of component. The other is the main part absorbed by the component transferred heat to make the component surface temperature increase.

The absorbed heat may be calculated according to the rate of the component temperature increased:

$$P_1 = mc_p\frac{\partial T}{\partial t} \tag{57}$$

where $\frac{\partial T}{\partial t}$ is the rate of the component temperature increased and m and c_p are the component mass and thermal capacity, respectively. It is therefore evident that the absorbed power would be estimated if it gained the rate of the component temperature increased. Another method to estimate the absorbed power is simulation based on the Monte Carlo method in the SRIM software which is an ion sputter simulation software (Shengyi and Xuhui 2010). With this method, it is also able to simulate the absorbed power P_1:

$$P_1 = \left(1 - \frac{Q_1}{Q}\right)P' \tag{58}$$

where Q is the absorbed energy and Q_1 is the sputter energy simulated. These two methods can validate each other to guarantee the model efficiency.

When the ion beam bombards the surface of component, a temperature gradient field is formed which may generate thermal stress. Here, a heat transfer model is constructed to analyze the temperature gradient distribution. Assuming that the radiated energy of ion source would be ignored, the component heat source is only ion beam which is a Gaussian function distribution as described in Fig. 5. The absorbed power may be described as

$$P_1 = \eta\iint_D Ae^{-\frac{r^2}{2\sigma^2}}ds \tag{59}$$

where r is the distance from the center of the Gaussian function as shown in Fig. 35. Equation 59 shows that the absorbed power is also a Gaussian distribution which

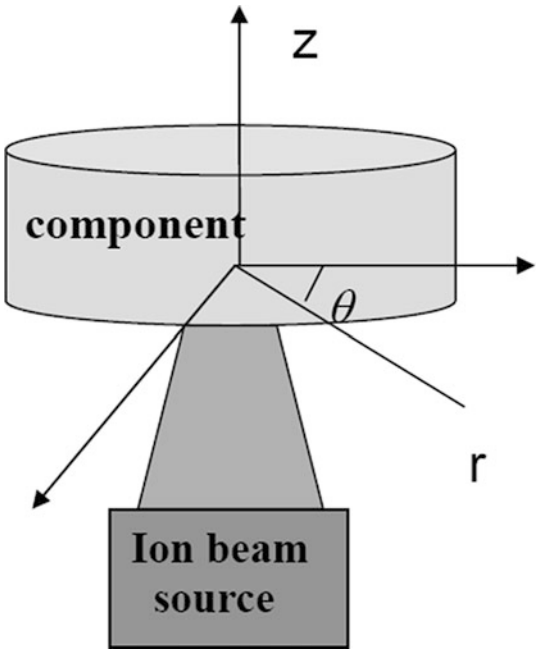

Fig. 35 Ion beam bombards component configuration

may generate nonuniformed thermal stress on the component. It is important to construct a suitable heat transfer model to analyze the thermal stress of component which is the key step to analyze and control the component thermal stress magnitude and the stress distribution.

As shown in Fig. 35, assuming that the ion beam bombards the center of the component along Z direction, the component heat transfer equation based on the Fourier heat transfer formulated in the cylinder coordinate frame is

$$\rho c_p \frac{\partial T}{\partial t} - k\left[\frac{\partial^2 T}{\partial r^2} + \frac{1}{r}\frac{\partial T}{\partial r} + \frac{\partial^2 T}{\partial z^2}\right] = 0 \tag{60}$$

where ρ, c_p and k are the material density, thermal capacity, and thermal conductivity, respectively. T is the interior temperature field distribution which is the function of radial coordinate r, axial coordinate z, and heated time t. $Ae^{-\frac{r^2}{2\sigma^2}}$ is the component area power density of ion beam.

Using the above temperature model, it can be analyzed and modeled that the temperature field and its temperature stress field of actual optical component figuring by ion beam. The experimental parameters are ion beam voltage 700 eV and its electro-current 60 mA, the diameter of ion beam 10 mm with ion diaphragm, and the vacuum 2.1×10^{-2} Pa. The BK7 experimental component is Φ 40 mm with thickness 10 mm. The reason to select a small component is that it is convenient to simulate the machining process. The actual component surface

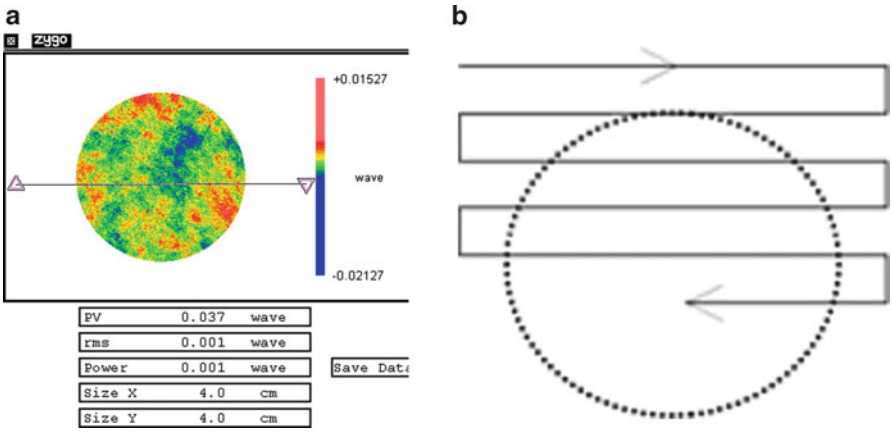

Fig. 36 Optical component machining By IBF

contour is shown in Fig. 36a, and its figured scanning is raster with 2 mm raster pitch shown in Fig. 36b.

Based on the data of actual surface contour, a simulation is done to get the temperature field and its temperature stress field by the above temperature model. The simulated results are shown in Fig. 37. In this figure, it can be seen that the machined component temperature field and its corresponding stress field are not uniform. It is known that the high-temperature gradient field on these materials will generate large thermal stress in the component, which apparently distorts its surface, and when the thermal stress is larger than the material mechanic stress limit of component, the component generates crack or break. The reasons to generate thermal stress are the rapid change of the component's temperature and high-temperature gradient. So, the troublesome and important problem is to select a suitable machining technique to control the temperature change rate and make temperature distribution uniformity in the IBF process.

A suitable machining technique method to make the component's temperature more even is to select a reasonable figuring method which can reduce the temperature gradient distribution, such as by designing a low-pass spatial frequency filter to process the component surface data measured by Zygo interferometer to only hold the component's low-frequency part and its middle- and high-frequency parts to be filtered. By this way, computer simulation results about the related temperature field and its thermal stress field shown in Fig. 38. Comparing Figs. 37 and 38, it is seen that the filtered IBF can gain the more even temperature field and thermal stress distribution. A final simulated result shows that the component maximum temperature is decreased about 10 % and its thermal stress is decreased about 22 %.

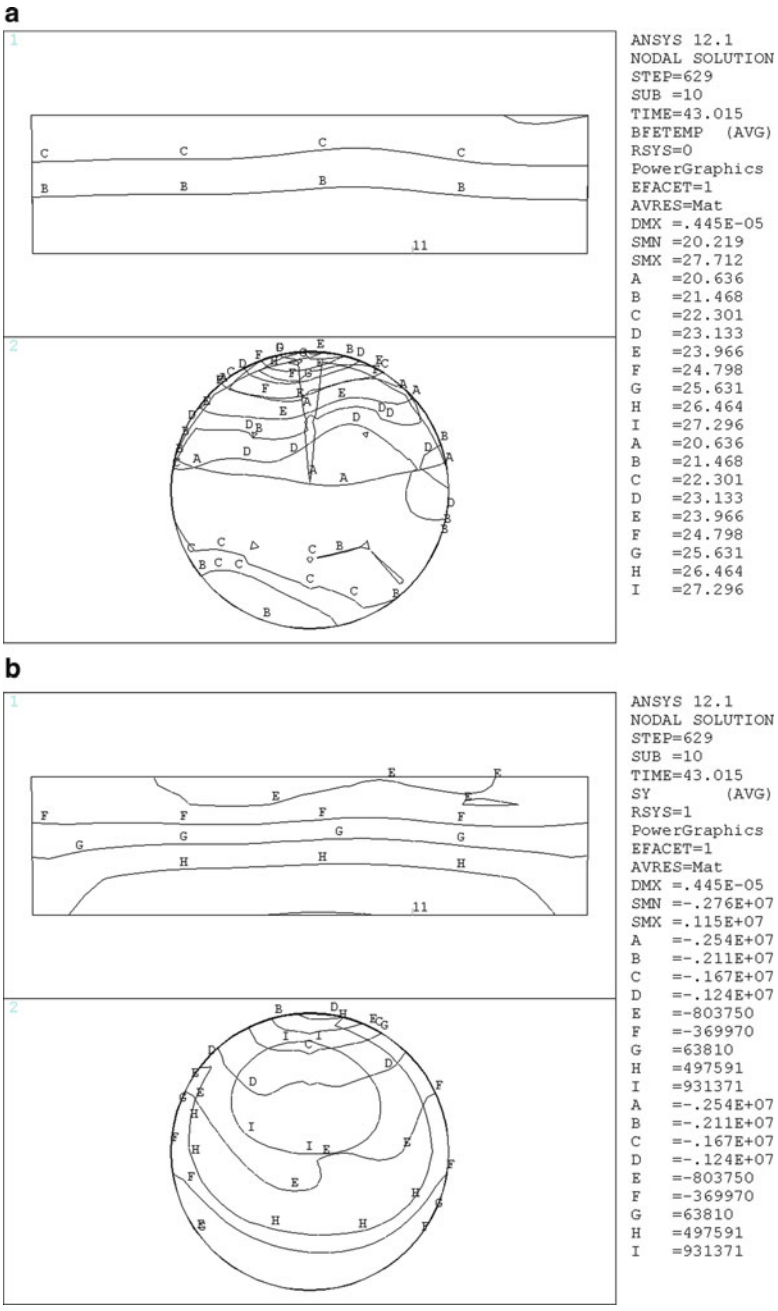

Fig. 37 Temperature field and its thermal stress field by IBF

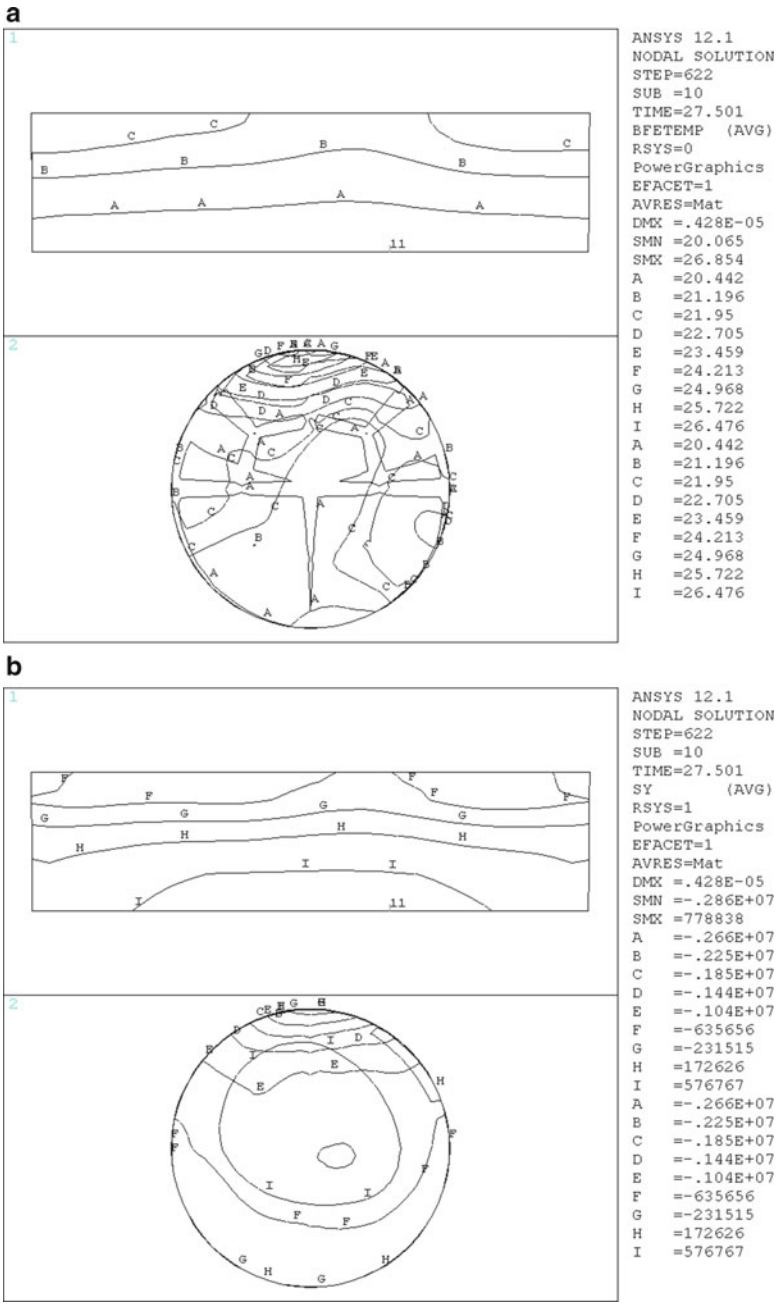

Fig. 38 Temperature field and its thermal stress field by filtered IBF

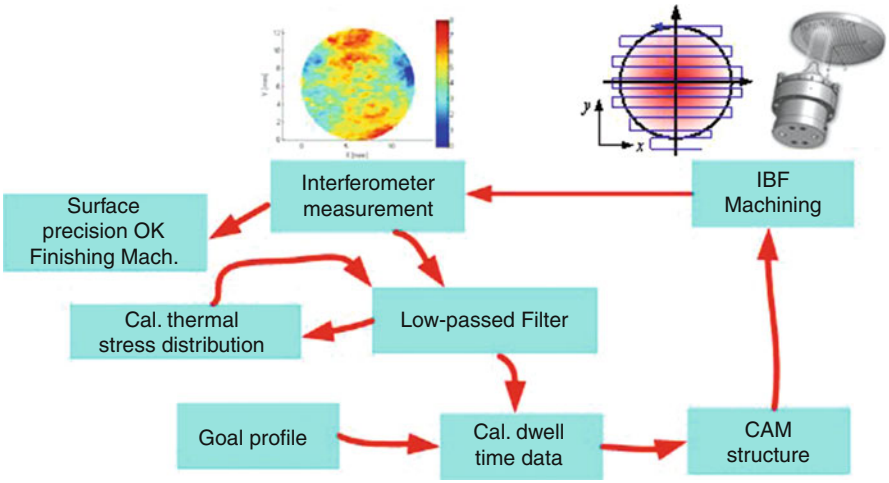

Fig. 39 Filtered ion beam figuring flow

Based on the above analysis, an ion beam figuring flow is set up for high thermal expansion and crystal optics as shown in Fig. 39.

Supersmooth Surface Figuring and Micro-roughness Evolution

The supersmooth surfaces of optical component is very precisely figured plane, spherical, and aspherical surfaces with the accuracies in depth down to the sub-nanometer level over the entire spatial wavelength range. The kinds of optics are very important for advanced DUVL, EUVL, and synchrotron. According to the Maréchal condition, the wave front of a diffraction-limited imaging system must achieve a deviation of λ/14 in the exit pupil (λ = operating wavelength). However, requirements for a lithographic system are even more demanding. For nowadays 193 nm and 13.5 nm systems, the expected residual wave front error of each optical element amounts to at least λ/20 or below: 0.20–0.28 nm RMS and 0.11–0.20 nm RMS, respectively (Bruning 2007). Similar or even smaller values hold for spatial frequencies higher than 1/1 mm as outlined elsewhere. The roughness of EUVL substrates is described with two different areas of spatial frequency:

MSFR = mid-spatial-frequency roughness between 1/mm and 1/μm and
HSFR = high-spatial-frequency roughness ranging from 1/μm to 50/μm.

It is proved that the ion beam figuring is a very useful tool to figure supersmooth optical surface. For example, supersmooth optical surface figure by IBF in Carl Zeiss, serial sphere with a diameter of 178 mm, rms = 0.13 nm, serial asphere with a diameter of 260 mm, rms = 0.19 nm (Weiser 2009). In China, our research group has also figured supersmooth optical surface shown in Fig. 40 using our designed IBF machine.

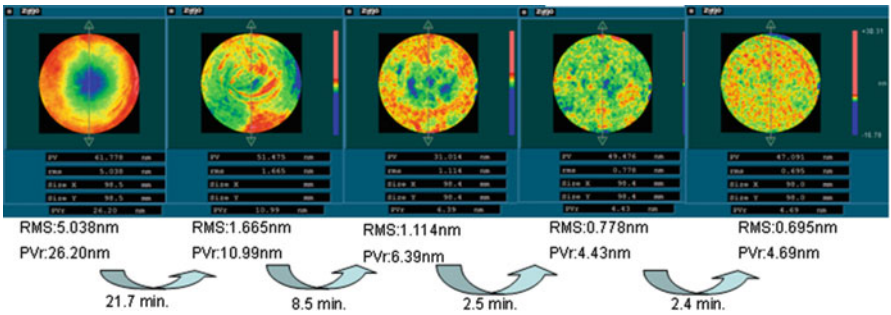

Fig. 40 Ion beam figuring results in NUDT

With ion beam to figure optical component, the micro-roughness is a regardful problem. Ion beam sputtering or ion beam erosion of surfaces can generate a diversity of surface topographies. Typically, during ion beam sputtering, the surface of the solid is far from equilibrium and a variety of atomistic surface processes and mechanisms become effective. It is the complex interplay of these processes that either tends to roughen (e.g., by curvature-dependent sputtering) or smoothen (e.g., by surface diffusion or viscous flow of surface atoms) the surface, which, finally, can result in the spontaneous formation of patterns (Frost et al. 2009).

Summary

In this chapter, it is known that IBF has five features and advantages: (1) high figuring precision, (2) highly predicable or stable, (3) noncontact figuring, (4) good material removal function, and (5) no or minimized support structure print effect. These make it to be an ideal machining method to figure ultraprecision optical component. Likely the conventional CCOS method, material removal function modeling, contouring algorithm, and realization of IBF process are its key technologies.

However, it has some shortcomings, such as working in vacuum chamber, component heating, difficulty of improving surface roughness because of the ion "sandblasting" effect at the atomic level, slow material removal rate, etc.

So, using IBF to machining optical component, the following problems would be deeply thought about:

1. The component material characteristics, if it is suitable to machining by IBF.
2. As one of the controllable compliant tools, it is well to adapt different asphere shape to improve its contour accuracy, but it is difficult to control its middle- and high-spatial-frequency error.
3. The ion "sandblasting" effect at the atomic level may make the surface roughness worse, so the ion beam parameter, total machining time or machining cycle, total removed material volume, etc., would be suitably selected.

References

Allen LN (1994) Progress in ion figuring large optics. Proc SPIE 2428:237–247
Allen LN, Keim RE (1989) An ion figuring system for large optic fabrication. Proc SPIE 1168:33–50
Allen LN, Roming HW (1990) Demonstration of an ion figuring process, in advanced optical manufacturing and testing. Proc SPIE 1333
Allen LN, Roming HW, Timothy SL (1991) Surface error correction of a Keck 10m telescope primary segment by ion figuring, advances in fabrication and metrology for optics and large optics. Proc SPIE 1531
Allen LN, John JH, Richard WW (1991) Final surface error correction of off-axis aspheric petal by ion figuring, advances in fabrication and metrology for optics and large optics. Proc SPIE 1543
Ando M, Numata A, Saito N, Taniguchi J (2004) Development of ion beam figuring system for mirror shape correction of minute area. In: The 3rd EUVL symposium, Tokyo
Bradley RM, Harper JME (1988) Theory of ripple topography induced by ion bombardment. J Vac Sci Technol A 6(4):2390–2395
Braunecker B, Hentschel R, Tiziani HJ (2007) Advanced optics using aspherical elements. SPIE Press, Bellingham
Bruning JH (2007) Optical lithography. 40 years and holding, SPIE 6520, 652004
Carnal C, Egert CM, Hylton KW (1992) Advanced matrix-based algorithm for ion beam milling of optical components. Proc SPIE 1752:54–62
Changjun Jiao, Shengyi Li, Xuhui Xie (2009) Algorithm for ion beam figuring of low-gradient mirrors. Appl Opt 48(21):4090–4096
Dai Yifan, Liao Wenlin, Zhou Lin, Chen Shanyong, Xie Xuhui (2010) Ion beam figuring of high slope surfaces based on figure error compensation algorithm. Appl Opt 49(34):6630–6636
Drueding TW (1995) Precision ion figuring system for optical components. PhD thesis, Boston University
Drueding TW, Bifano TG, Fawcett SC (1995) Contouring algorithm for ion figuring. Precis Eng 17:10–21
Fang CZ, Xiao DY (1998) Process identification. Tsinghua University Press
Fawcett SC (1994) Development of an ion beam figuring system for centimeter scale optical components. Proc SPIE 2263:164–167
Frost F, Fechner R, Ziberi B, Ollner JV, Flamm D, Schindler A (2009) Large area smoothing of surfaces by ion bombardment: fundamentals and applications. J Phys Condens Matter 21
Fruit M, Schindler A, Hansel T (1999) Ion beam figuring of SiC mirrors provides ultimate WFE performances for any type of telescope. Proc SPIE 3739:142–154
Gailly P, Collette JP, Tockj P et al (1999) Ion beam figuring of small BK7 and Zerodur optics: thermal effects[C]. In: The Europe conference on optical fabrication and testing, Berlin
Gale AJ (1978) Ion machining of optical components. In: Optical society of America annual meeting conference proceedings
Ghigo M, Citterio O, Conconi P, Mazzoleni F (2001) Ion beam figuring of nickel mandrels for x-ray replication optics In: Andreas K.Freund et al. Advances in X-ray optics. SPIE Vol 4145 (2001):28–36
Ghigo M, Cornelli S, Canestrari R, Garegnani D (2009) Development of a large ion beam figuring facility for correction of optics up to 1.7 m diameter. Proc SPIE 7426
Haensel T, Seidel P, Nickel A, Schindler A (2006) Deterministic ion beam figuring of surface errors in the sub-millimeter spatial wavelength range[C]. In: Proceedings of EUSPEN, Baden/Vienna
Haensel T, Nickel A, Schindler A (2008) Ion beam figuring of strongly curved surfaces with a (x,y,z) linear three-axes system. Plasmonics and metamaterials, OSA technical digest (CD) (Optical Society of America, 2008), JWD6
Ion beam finishing technology for high precision optics production, NTGL-Nanotechnologie Leipzig GmbH. http://www.ntgl.de. Accessed 9 Jan 2003

Kaufman HR, Reader PD, Isaacson GC (1977) Ion sources for ion machining applications. AIAA J 15(6):843–847
Lin Zhou, Xie Xuhui, Dai Yifan, Jiao Changjun, Shengyi Li (2007) Ion beam figuring system in NUDT. Proc SPIE 67224A:1–6
Lin Zhou, Yifan Dai, Xuhui Xie, Changjun Jiao, Shengyi Li (2008) Analysis of Correcting Ability of Ion Beam Figuring. Key Eng Mater 2008:364–366, P470–475
Lin Zhou, Yifan Dai, Xuhui Xie, Shengyi Li (2009) Frequency-domain analysis of computer-controlled optical surfacing processes. Sci Ch Ser E-Technol Sci 53(7):2061–2068
Lin Zhou, Yifan Dai, Xuhui Xie, Shengyi Li (2010) Optimum removal in ion beam figuring. Precis Eng 34:474–479
Lucy LB (1974) An iterative technique for the rectification of observed distribution. Astron J 79:745–754
Meinel AB, Bushkin S, Loomis DA (1965) Controlled figuring of optical surfaces by energetic ionic beams. Appl Opt 4:1674
Molina R, Nunez J, Cortijo F, Mateos J (2001) Image restoration in astronomy: a Bayesian perspective. IEEE Signal Process Lett 18:11–29
Nelson J (2010) DRAFT ion figuring thermal considerations, TMT. PSC.TEC. 10.006.REL02
Particle interactions with matter. http://www.srim.org/
Richardson WH (1972) Bayesian-based iterative method of image restoration. J Opt Soc Am 62:55–59
Roland G (2010) New challenges in precision optics astronomy: from VLT to ELT microlithography: from DUV to EUV, keynote, AOMATT, Dalian
Schindler A, Haensel T, Zeuner M, Seidenkranz G (2000) Ion beam figuring and ion beam polishing production tools – processing technology included – for customized solutions. Trends Opt Photonics Opt Fabr Test 42:135–137, xii+165
Shanbhag PM, Feinberg MR, Sandri G, Horenstein MN, Bifano TG (2000) Ion-beam machining of millimeter scale optics. Appl Optics 39:599–611
Shengyi Li, Xuhui Xie (2010) Research on controllable compliant tools (CCT) theory and technology. Proc SPIE 7655:765509-1:765509-9
Sigmund P (1973) A mechanism of surface micro-roughening by ion bombardment. J Mater Sci 8:1545–1553
Tock JP, Collette JP, Gailly P, Kampf D (1999) Figuring sequences on a super-smooth sample using ion beam technique. Proc SPIE 3739:132–141
Weiser M (2009) Ion beam figuring for lithography optics. Nucl Instrum Methods Phys Res B 267
Wilson SR (1987) Ion beam figuring of optical surfaces. Master's thesis, University of New Mexico
Wilson SR, McNeil JR (1987) Neutral ion beam figuring of large optical surface. Proc SPIE 818:320–324
Wilson SR, Reicher DW, McNeil JR (1989) Surface figuring using neutral ion beams. In: Proceedings of the SPIE – the international society for optical engineering |proceedings of the SPIE – the international society for optical engineering, vol 966, pp 74–81
Xie xuhui, Gu Wen-hua, Zhou lin (2009) Study on machining small precision optical component using thin ion beam. J Natl Univ Def Technol 31:10–14
Xuhui Xie, Lin Zhou, Yifan Dai, Shengyi Li (2011) Ion beam machining error control and correction for small scale optics. Appl Opt 50(27):5221–5227
Xuhui Xie, Yu Hao, Lin Zhou, Yifan Dai, Shengyi Li (2012) High thermal expansion optical component machined by IBF. J Opt Eng 51(1):013401-1–013401-7
Yuan Zheng, Dai Yifan, Xie Xuhui, Zhou Lin (2011) Ion beam figuring for ultra-precise optics. In: Key Engineering Materials. 2012, 516:19–24
Zhou lin, Dai yifan, Xie xuhui (2007) Model and method to determine dwell time in ion beam figuring. Nanom Technol Precis Eng 5(2):107–112